ARMY RESEARCH LABORATORY

# Plastic Flow and Failure In HY100, HY130 and AF1410 Alloy Steels Under High Strain Rate and Impact Loading Conditions

A.M. Rajendran, H.R. Last, and R.K. Garrett, Jr.

ARL-TR-687

March 1995

The findings in this report are not to be construed as an official Department of the Army position unless so designated by other authorized documents.

Citation of manufacturer's or trade names does not constitute an official endorsement or approval of the use thereof.

Destroy this report when it is no longer needed. Do not return it to the originator.

# REPORT DOCUMENTATION PAGE

Form Approved
OMB No. 0704-0188



| 1. AGENCY USE ONLY *(Leave blank)* | 2. REPORT DATE | 3. REPORT TYPE AND DATES COVERED |
|---|---|---|
| | March 1995 | |

**4. TITLE AND SUBTITLE**
Plastic Flow and Failure In HY100, HY130 and AF1410 Alloy Steels Under High Strain Rate and Impact Loading Conditions

**5. FUNDING NUMBERS**

**6. AUTHOR(S)**
A.M. Rajendran, *H.R. Last, and R.K. Garrett, Jr.

**7. PERFORMING ORGANIZATION NAME(S) AND ADDRESS(ES)**
Army Research Laboratory
Watertown, MA 02172-0001
ATTN: AMSRL-MA-PD

**8. PERFORMING ORGANIZATION REPORT NUMBER**
ARL-TR-687

**9. SPONSORING/MONITORING AGENCY NAME(S) AND ADDRESS(ES)**

**10. SPONSORING/MONITORING AGENCY REPORT NUMBER**

**11. SUPPLEMENTARY NOTES**
*H.R. Last and R.K. Garrett, Jr., Naval Surface Warfare Center, Silver Spring, MD 20903-5000

**12a. DISTRIBUTION/AVAILABILITY STATEMENT**
Approved for public release; distribution unlimited.

**12b. DISTRIBUTION CODE**

**13. ABSTRACT** *(Maximum 200 words)*

This report presents the results from impact experiments, constitutive/failure modeling, and metallurgical failure analyses for three steels: HY100, HY130, and AF1410. The main objectives of this effort are: 1) to obtain fundamental engineering data in terms of stress-strain curves up to failure at different temperatures and strain rates, 2) to evaluate the observed differences in the macroscopic behaviors through microscopic metallurgical studies, and 3) to describe the flow and failure behaviors using already available material strength and spall models. The high strain rate and impact experiments considered are the split Hopkinson bar (SHB) and the planar plate impact tests, respectively. In addition, the baseline data include quasi-static (QS) tests at low strain rates. The QS and SHB data provide stress-strain curves at different strain rates and temperatures. The experimental data illustrate the effects of two important loading parameters (strain rate and temperature) on the flow and failure behaviors of HY100, HY130, and AF1410 steels.

| 14. SUBJECT TERMS | 15. NUMBER OF PAGES |
|---|---|
| Ductile Failure, High Strain Rate, Impact, Constitutive Models, Failure Models | 67 |
| | 16. PRICE CODE |

| 17. SECURITY CLASSIFICATION OF REPORT | 18. SECURITY CLASSIFICATION OF THIS PAGE | 19. SECURITY CLASSIFICATION OF ABSTRACT | 20. LIMITATION OF ABSTRACT |
|---|---|---|---|
| Unclassified | Unclassified | Unclassified | UL |

## Contents

Page



## Figures

Page

Page

Page



## Tables

Page

# 1. Introduction

The need for high strength, high toughness, and weldable structural steels was the driving force behind the development of the HY-steels. The U.S. Air Force, interested in structural steels with needs for even higher strength while maintaining toughness, developed AF1410. These high strength, high toughness steels are used in demanding applications involving high rates of loading (landing gear, armor). Consequently, for design purposes, a complete understanding of the material constitutive response is required. Enhanced understanding of the high strain rate response of HY100, HY130, and AF1410 steels will lead to realistic and accurate material strength and damage models for armor/anti-armor analyses using advanced finite element/difference computer programs.

This report presents the results from impact experiments, constitutive/failure modeling, and metallurgical failure analyses for three steels: HY100, HY130, and AF1410. The main objectives of this effort are: 1) to obtain fundamental engineering data in terms of stress-strain curves up to failure at different temperatures and strain rates, 2) to evaluate the observed differences in the macroscopic behaviors through microscopic metallurgical studies, and 3) to describe the flow and failure behaviors using already available material strength and spall models. The high strain rate and impact experiments considered are the split Hopkinson bar (SHB) and the planar plate impact tests, respectively. In addition, the baseline data include quasi-static (QS) tests at low strain rates. The QS and SHB data provide stress-strain curves at different strain rates and temperatures. The experimental data illustrate the effects of two important loading parameters (strain rate and temperature) on the flow and failure behaviors of HY100, HY130, and AF1410 steels.

The widely-used Johnson-Cook (JC) [1] model and the thermodynamically-consistent viscoplastic constitutive model of Bodner and Partom (BP) [2] were considered in the modeling effort. The constants for these models were determined from room and high temperature stress-strain curves at various strain rates. While the plastic flow behaviors were characterized by the JC and BP models, the dynamic ductile failure mechanisms were modeled using the physically based model developed by Rajendran, Dietenberger, and Grove [3] (RDG). The RDG model was initially implemented into the 1986 version of the EPIC finite element code [4]. Recently, Grove and Rajendran [5] successfully implemented the RDG model into the 1992 version of the EPIC code [6]. Using this newer-version EPIC code, the material constants for the RDG model were determined by matching the computed spall signals with the stress gauge measured spall signals from the plate impact experiments.

Section 2 describes the material invenstigated including physical and mechanical properties of HY100, HY130, and AF1410 steels. The SHB and plate impact test configurations are briefly described in Section 3. The compressive strengths at high strain rate as determined from the plate impact tests are also tabulated in this section. Section 4 discusses the results from the QS and SHB tests. The strain hardening, strain rate hardening, and thermal softening behaviors at room and elevated temperatures are

evaluated. Section 4 also includes a discussion on the observed microstructural differences between the three steels. For completion, the JC and BP strength models are briefly discussed in Section 5. The void nucleation and growth based RDG failure model is also briefly presented in this section. Section 6 summarizes the results and suggests additional work.

## 2. Material Description

The HY100 and HY130 steels were designed for high strength, high toughness applications where weldability is required. Some applications include submarine pressure hulls, component sections in hulls of U.S. Navy surface ships, and machinery and shock test platforms. The AF1410 steel has a higher strength than the HY100 and HY130 steels. Similar to the HY-steels, AF1410 was developed for structural applications where the combination of high strength and high fracture toughness is required.

### 2.1 Composition

The composition of each steel is presented in Table 1. HY100 and HY130 are low alloy, low carbon (<0.2 wt% C) steels. AF1410 is a higher alloy, low carbon steel. Compared to the HY-steels, the levels of the major alloying element additions (e.g. Ni, Cr, Mo) are significantly higher in AF1410. AF1410 also has ~14 wt% Co added; there is no Co addition in the HY-steels. The carbon content for AF1410 is higher than HY130 and the same as HY100. Also, the manganese and silicon levels are significantly lower in the AF1410 than in either HY-steel.

### 2.2 Microstructure

The microstructure of each of these steels consists of tempered lath martensite. The martensitic laths tend to align themselves parallel to one another in areas of the parent austenite grain. These regions of parallel laths are referred to as packets. The packet structure is important in determining mechanical properties and fracture behavior [7]. Tempering the martensite results in the precipitation of carbides at interlath boundaries, on dislocations, or at both sites. The combination of the martensitic structure with the carbides results in the high strength, high toughness characteristics of these steels. Presented in Figure 1 are optical micrographs of the microstructures of the three steels. The microstructures of HY100 and HY130 exhibit a tempered martensitic structure with carbides (mainly $Fe_3C$) decorating the prior austenite boundaries as well as the martensitic interlath boundaries [8]. As a result of composition and tempering practice, the carbides present in HY100 and HY130 are expected to coarsen at the tempering temperature employed. The AF1410 microstructure also consists of tempered martensite. Compared to the microstructures of HY100 and HY130, AF1410 consists of what appears to be a finer martensitic lath structure with the martensitic packets not as clearly defined (Figure 1). Unlike the HY-steels, AF1410 is a secondary hardening steel. Instead of being strengthened by the precipitation of mainly $Fe_3C$ as in the case of the HY-steels, AF1410 is strengthened by a finer distribution of $M_2C$ (where M = Mo, Cr) [9].

### 2.3 Physical Properties

Presented in Table 2 is a list of physical properties for HY100, HY130 and AF1410. Such properties are typically required for the material modelling efforts. This list is a compilation from various sources and provides realistic values of the cited properties for these steels. The sources of the data are

identified in Table 2. When these properties are required for a specific product form, the most accurate approach would be to directly measure them for the product of interest.

**Table 1. Actual composition of steels used in this investigation.**

| STEEL | COMPOSITION (wt%) | | | | | | | | |
|---|---|---|---|---|---|---|---|---|---|
| | Ni | Co | Cr | Mo | C | Mn | S | P | Si |
| HY100 | 2.40 | --- | 1.27 | 0.23 | 0.16 | 0.34 | 0.003 | 0.006 | 0.26 |
| HY130 | 4.92 | --- | 0.53 | 0.45 | 0.11 | 0.76 | 0.003 | 0.003 | 0.30 |
| AF1410 | 10.23 | 14.35 | 2.05 | 1.03 | 0.16 | 0.02 | 0.003 | 0.003 | 0.01 |

**Table 2. Properties of the three steels compiled from various sources.**

| Property | HY-100 | HY-130 | AF1410 |
|---|---|---|---|
| Yield Strength min/max, ksi (MPa) | 100/120[a] (689/827) | 130/150[b] (896/1034) | 215/---[c] (1482/---) |
| $K_{Ic}$,Fracture Toughness, min ksi$\sqrt{in}$ (MPa$\sqrt{m}$) | 160[d] (176) | 140[d] (154) | 120[e] (132) |
| Modulus of Elasticity, ksi (MPa) | 29 to 31 x$10^3$ (20 to 21 x$10^4$) | 29 to 30 x$10^3$ (20 to 20.7 x$10^4$) | 28 to 30 x$10^3$ (19.3 to 20.7 x$10^4$)[f] |
| Density, lb/in$^3$ (kg/m$^3$) | 0.280[g] (7746) | 0.285[g] (7885) | |
| Melting Temperature, K (°C) | 2768[g] (1793) | 2768[g] (1793) | 2768[h] (1793) |
| Poisson's Ratio ($\upsilon$) | 0.3[g] | 0.3[g] | 0.3[h] |
| Shear Modulus, Msi (GPa) | 11.2 to 11.9 (77 to 82) | 11.2 to 11.5 (77 to 79) | 10.8 to 11.5 (74 to 79) |
| Bulk Modulus, Msi (GPa) | 24.2 to 25.8 (167 to 178) | 24.2 to 25 (167 to 172) | 23.3 to 25 (161 to 172) |

a USS properties card
b MIL-S-24371B(SH)
c McDonnel MMS-214 REV C AMD 1
d Calculated from $J_{Ic}$ values per conversation w/M. Vassilaros at DTRC, ($K_{Ic} = \sqrt{(J_{Ic}*E)}$)
e reported value for transverse specimen on bar
f Technical Report ARCCB-TR-91021
g NSWC TR 88-252
h assumed

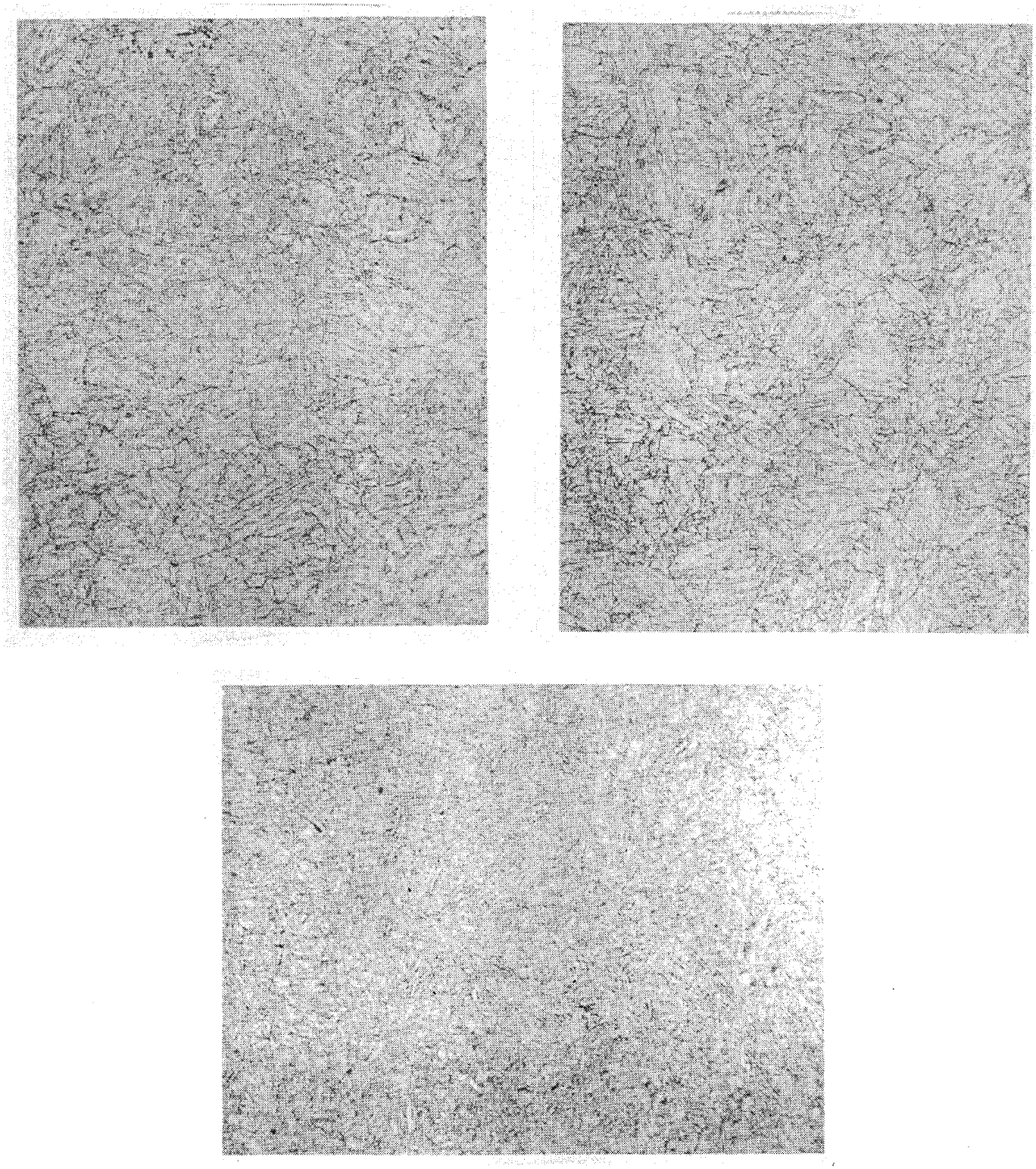

Figure 1. Optical photomicrographs showing the tempered martensitic structures of a) HY100, b) HY130, and c) AF1410 steels.

## 3. Experiments

The main objectives of the high strain rate testing are: (1) to determine the Hugoniot elastic limit (HEL), the spall strength, and the variation of yield strength with respect to strain rate at room and elevated temperatures, (2) to obtain the deformation and flow stress at large strains from the analysis of high speed photographs of dynamically deforming specimens, and (3) to obtain stress-time histories (wave profiles) from stress gauges for failure modeling. To accomplish these objectives, two test configurations were considered: split Hopkinson bar and plate impact. The experiments were performed at the University of Dayton Research Institute, Dayton, Ohio. The split Hopkinson bar (SHB) experiments provide stress-strain data for metals over a strain rate range of 500 - 2000/sec. Variation of flow strength with respect to strain rate can be constructed from these data. Parameters for the Johnson-Cook [1] and Bodner-Partom [2] strength models were determined by adjusting the constants to accurately reproduce the QS and SHB stress-strain curves up to the onset of necking. The data from the high speed camera pictures were useful in obtaining stress-strain data at large strains beyond the onset of necking using the Bridgman analysis as demonstrated by Rajendran and Bless [10].

To characterize the high strain rate behaviors of HY100, HY130 and AF1410 steels, several quasi-static and split Hopkinson bar tensile tests were performed at room and elevated temperatures. Two strain rates (0.001/sec and 1300/sec) and two temperatures (23°C and 400°C) were considered. The strain rate in all the quasi-static tests was 0.001/sec. All the specimens were tested to failure and complete stress-strain curves up to failure were obtained from these tests. The test matrix is given in Table 3.

**Table 3. Quasi-static and split Hopkinson bar test matrix**

| Materials | Quasi-static | | SHB | |
|---|---|---|---|---|
| | Room | 400°C | Room | 400°C |
| HY100 | 3 | 3 | 4 | 4 |
| HY130 | 3 | 2 | 10 | 4 |
| AF1410 | 4 | 3 | 9 | 4 |

### 3.1 Split Hopkinson Bar

A schematic of the split Hopkinson bar (SHB) and the typical dimensions of a standard tensile specimen are shown in Figure 2. This apparatus consists of a striker bar that is made to impact end-to-end onto a pressure bar. The impact produces a stress wave in the pressure bar whose duration is twice the acoustic transit time of the striker bar. The specimen is placed at the other end of the pressure bar (bar no. 1) as shown in Figure 2. The specimen is also connected to the transmission bar (bar no. 2). The stress wave that travels down the pressure bar is partially transmitted and partially reflected by the

specimen. The reflected and transmitted waves are detected by the strain gages on the pressure and transmission bars, respectively. Analysis of the strain-gage signals yields the load and displacement history of the specimen [11].

For tensile tests at room temperature, a collar is placed around the threaded end of the specimen, and the specimen is screwed into the pressure and transmission bars. The initial compression wave is transmitted through the collar. This compression wave reflects as a tensile wave from the free end of the second bar. When the tensile wave returns to the specimen, the collar falls away and only the specimen sustains the tensile load. The data from the Hopkinson bar strain gages are used to calculate engineering stress and strain in the sample, which is then converted to true stress and strain until the onset of localized deformation (necking) using the conventional relationships.

To obtain SHB data at elevated temperatures, an induction coil heating technique was employed [12]. In this technique, the specimen to be heated is surrounded by an induction coil which carries a high frequency current. The coil diameter is kept larger than the Hopkinson bar diameter (12.7 mm) by only about 3 mm. A ceramic collar is used instead of a metallic one to transmit the initial compressive pulse. The collar is made of Alumina AD-995 which has an acoustic impedance very close to that of the bar. This impedance matching ensures a smooth passage of the stress wave from the pressure bar to the transmission bar through the ceramic collar. The temperature of the specimen just prior to loading was measured by a thermocouple inserted through a hole drilled in the ceramic collar.

The loading duration in the SHB dynamic tests is typically between 100 - 300 microseconds. In contrast, the duration of a quasi-static test is about 8-10 minutes. Therefore, the specimen is exposed to the test temperature for a longer time in a quasi-static test than in a conventional SHB test. In this study, the SHB specimens were exposed to the test temperature for about the same duration of time as in the quasi-static tests.

An IMACON high speed camera was employed to obtain data for ductile necking evolution in the three steels. Rajendran and Bless [10] described the use of such data to correct the engineering stress-strain relationship beyond the onset of necking. The measured radius of curvature of the neck profile and the minimum radius from the high speed photographs are used to calculate the Bridgman correction factors [13]. Using the Bridgman relationship, the SHB stress-strain curves beyond the onset of necking can be constructed.

### 3.2 Plate Impact

The plate impact experiment is the most commonly used configuration for studying dynamic tensile (spall) failure in materials at very high strain rates. In the plate impact test, a flat flyer plate is made to impact against a target plate at a high velocity. The diagnostic measurements usually involve a VISAR to measure the particle velocity history or piezo-resistive stress gauges to measure the stress

history at the target and back plate interface. The flyer and target may be of the same or different material. Compressive stresses are produced and transmitted immediately from the plane of impact to the adjacent stress free areas of the material in the form of a stress pulse. Figure 3 shows a schematic of the plate impact test configuration, along with a typical free surface velocity history is shown in Figure 3.

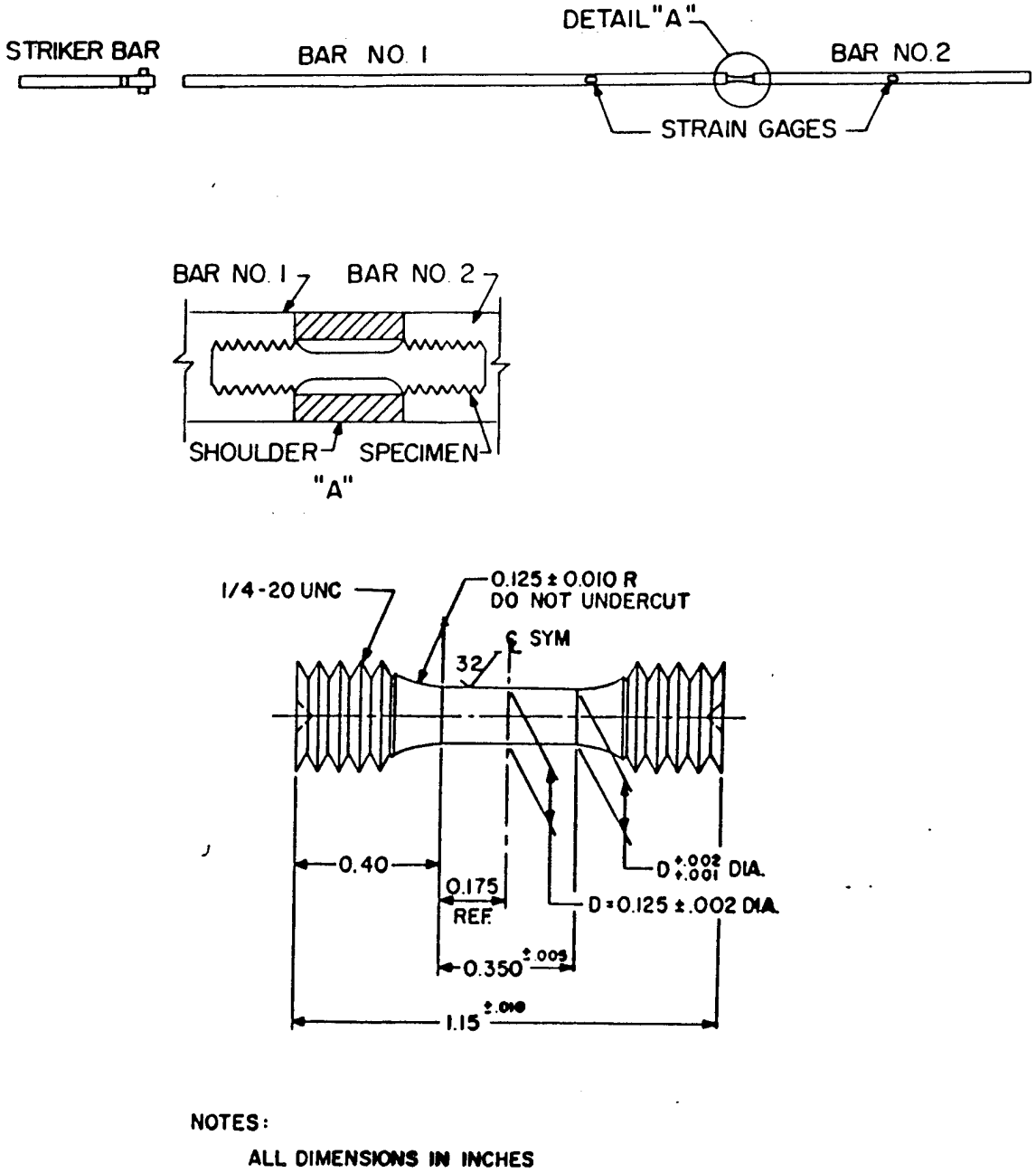


Figure 2. A schematic of the split Hopkinson bar test set-up and dimensions of the tensile specimen.

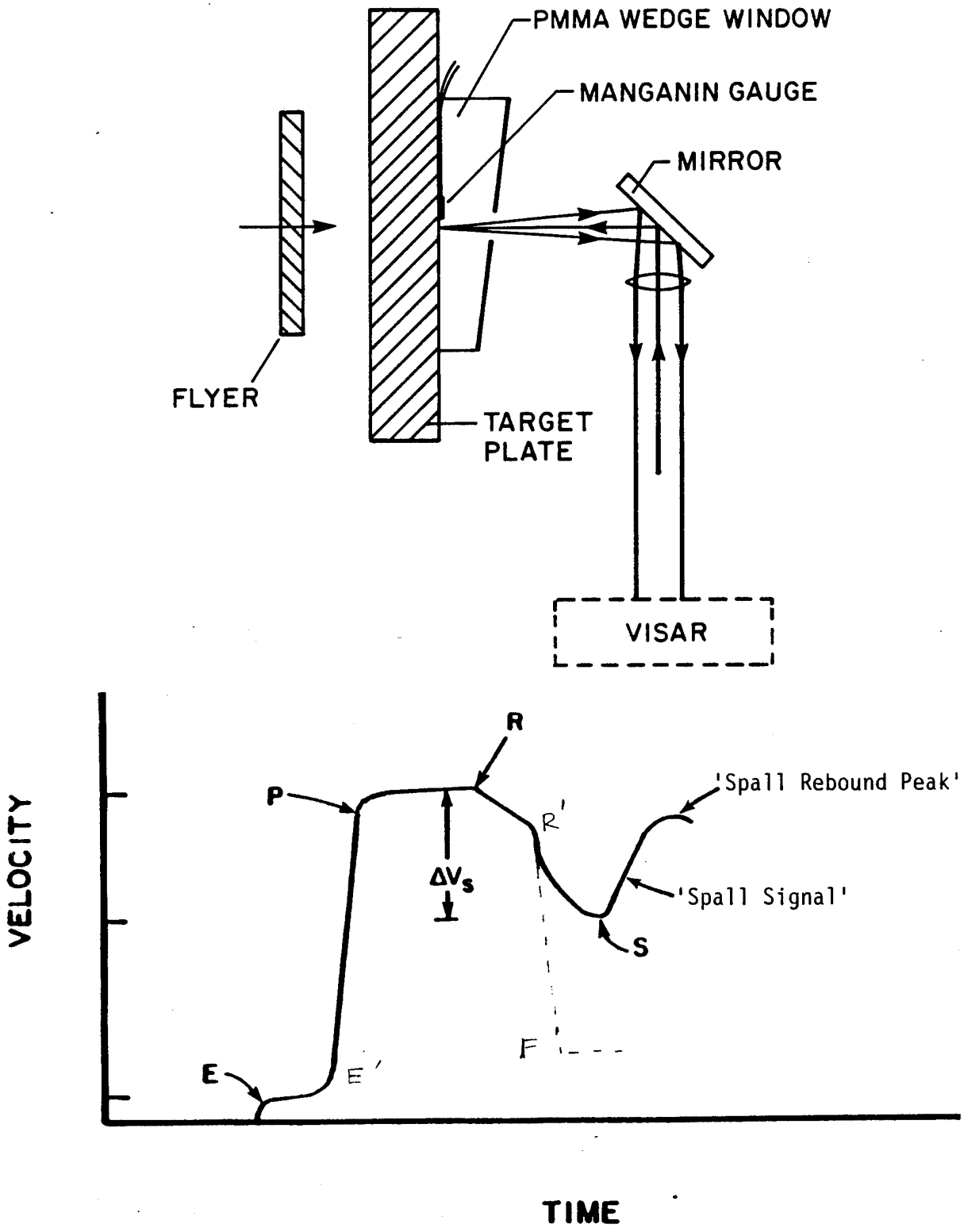


Figure 3. A schematic of plate impact test configuration and a typical VISAR measured velocity versus time profile.

The portion of the velocity history indicated by the letter E represents the arrival of an elastic shock wave from the impact plane. The material particles are compressed elastically (E-E′) until the relatively slow moving plastic shock wave arrives at the free surface. Typically, both the shape and time duration of the portion E-E′ depend on the strain rate sensitivity of the material and thickness of the target plate.

For engineering calculations, the average velocity level between the points E and E′ is usually defined as the velocity at the HEL, $V_{HEL}$. Using this experimental value, the stress at the HEL ($\sigma_{HEL}$) is calculated from the relationship $\sigma_{HEL} = \frac{1}{2}\rho c V_{HEL}$, where $\rho$ is the material density, c is the elastic sound wave speed, and $V_{HEL}$ is the velocity at the HEL measured at the target's free surface. This expression is valid only under symmetric impact conditions, that is, when the target and flyer are of the same material.

The high strain rate yield strength, $Y_o$, can then be calculated as,

$$Y_0 = \frac{\sigma_{HEL}}{\left[\frac{k}{2G} + \frac{2}{3}\right]} \tag{1}$$

where G is the shear modulus and K is the bulk modulus. When the plastic shock wave arrives at the target's free surface, this wave takes the particle velocity to the peak level defined between points P and R. Later, the elastic release wave from the back surface of the flyer plate arrives at point R, and the velocity drops to R′. The plastic release wave from the flyer reaches the target's free surface and drops the velocity further to F. In general, in modeling, the level E-E′ and the wave structure around the HEL are sensitive to the constitutive relations (strength models); however, the slopes and peak of the VISAR signal depend primarily on the pressure-volume relationship (equation of state).

Depending on the severity of the impact, the bulk material (target) can spall and a stress-free fracture surface (spall plane) is created in the target. When the spall plane separates inside the target, the stresses relax to zero, and hence, a compressive shock wave is generated. This shock wave arrives at point S, as shown in the typical VISAR signal. The material particle velocity history follows the solid line (recompression). The signal beyond point S is often denoted as the "spall signal." This spall signal is most often used in the estimation and calibration of failure model parameters.

Plate impact experiments on the three steels (HY100, HY130, and AF1410) were performed at the University of Dayton Research Institute and details of the tests are given in Table 4. The Hugoniot elastic limits (HEL) for these various metals were determined and are tabulated in Table 5. The compressive flow strength of AF1410 was much higher than the strengths of HY100 and HY130 steels

at extremely high strain rates (>$10^4$/s). The manganin-gauge measured stress-time histories are used in the failure modeling of these steels. The RDG model constants are often calibrated by matching the numerically calculated stress histories with the experimentally measured stress histories.

**Table 4. Plate impact tests**

| Shot No. | Velocity (m/s) | Flyer Plate | | Target Plate | |
|---|---|---|---|---|---|
| | | Material | Thickness (mm) | Material | Thickness (mm) |
| 7-1686 | 504 | HY130 | 4.0 | HY130 | 8.0 |
| 7-1687 | 715 | HY130 | 4.0 | HY130 | 8.0 |
| 7-1688 | 488 | HY130 | 3.0 | HY130 | 8.0 |
| 7-1690 | 494 | HY100 | 3.0 | HY100 | 8.0 |
| 7-1692 | 481 | HY100 | 4.0 | HY100 | 8.0 |
| 7-1693 | 779 | HY100 | 2.0 | HY100 | 8.0 |
| 7-1691 | 484 | HY100 | 4.0 | HY100 | 8.0 |
| 7-1695 | 672 | AF1410 | 4.0 | AF1410 | 8.0 |
| 7-1696 | 668 | AF1410 | 3.0 | AF1410 | 8.0 |
| 7-1697 | 668 | AF1410 | 2.0 | AF1410 | 8.0 |
| 7-1698 | 536 | AF1410 | 3.0 | AF1410 | 7.6 |

**Table 5. HEL and compressive strength of AF1410, HY100, and HY130 steels**

| MATERIAL | HEL (kbar) | Y (kbar) |
|---|---|---|
| AF1410 Steel | 36.0 | 20.9 |
| HY100 Steel | 16.0 | 9.3 |
| HY130 Steel | 23.0 | 13.3 |

# 4. Experimental Results and Discussions

In this section, the effects of strain rate and temperature on the strain hardening, strain rate hardening, and strain at failure are presented for HY100, AF1410, and HY130 steels. The discussions also focus on the role of metallurgical effects on the material behavior modification at elevated temperature and high strain rate.

To identify any difference in quasi-static stress-strain behavior due to specimen orientation, the engineering stress-strain curves for longitudinal (L) and transverse (T) specimens at two different temperatures (23°C and 400°C) were obtained for AF1410 steel. The differences due to specimen orientation were found to be relatively insignificant at both temperatures, except for a small difference in the post-yield region. A similar trend was observed under high strain rate loading conditions for the two orientations at both room and elevated temperatures. The absence of any orientation effect was previously established for the HY100 and HY130 steels [14].

## 4.1 Room Temperature (RT)

### a. Strain Hardening

The QS ($10^{-3}$/s) and SHB ($10^{+3}$/s) engineering stress-strain curves for the three steels are compared in Figure 4. The actual SHB data is presented in the plots. The stress-strain data for HY100 and HY130 were relatively noisier than AF1410. However, the overall shape of the average curve for HY100 followed the QS curve. Among the three steels, HY100 was the most strain hardening material and AF1410 was the least strain hardening material.

The stress-strain curves for AF1410 exhibited continually decreasing flow stresses with respect to increasing strain. Immediately beyond the onset of plastic yielding, the flow stresses at both low and high strain rates start decreasing, indicating the onset of necking in AF1410. Therefore, it was not possible to determine the strain hardening behavior of AF1410 from these tensile tests. In general, the strain rate effect was negligible on the strain hardening behavior of these metals. In BCC metals, the strain hardening is not usually influenced by the strain rate. The slope of the stress-strain curve at any given strain value prior to the onset of necking is independent of strain rate.

### b. Failure Strain

The scatter in the failure strain measurements for quasi-static and SHB tests is also shown in Figure 4. The strain to failure was consistently larger under dynamic loading conditions for the three steels. Rajendran and Fyfe [15] and Regazzoni and Montheillet [16] found a similar trend in copper (fcc metal) and concluded that the increase in failure strain is due to inertial effects. Adiabatic shear banding and inertia impose competing effects on the failure strain.

The analyses of these investigators indicated that inertia plays the dominant role in delaying the onset and progression of necking. The present experimental results further confirm the effects of inertia in high strength steels (bcc metals). Under high strain rate loading, the failure strain increased by about 30% in HY100, 15% in HY130, and 8% in AF1410.

**c. Strain Rate Hardening**

The HY100 steel exhibited strain rate hardening. Figure 4 for HY100 shows higher flow stresses in the SHB tests at strain rates about 1500/s than in the quasi-static tests at 0.001/s. Other investigators [14] have also found rate dependency in this steel. The AF1410 and HY130 steels did not exhibit any rate dependency in the strain rate regime between $10^{-3}$/sec and $10^{3}$/sec as can be seen from the plots in Figure 4. The average SHB stress-strain curves are very similar to the QS curves for these two steels.

## 4.2 High Temperature (400°C)

The room temperature (RT) and high temperature (HT) stress-strain curves are compared in Figure 5 for the three steels under quasi-static loading. The thermal softening in AF1410 was relatively higher than in HY100 and HY130. At elevated temperatures, the onset of necking occurred immediately upon plastic yielding in all three steels. Interestingly, the strain to failure was significantly lower at HT.

In Figure 6, the stress-strain curves from the SHB tests are plotted for both RT and HT conditions. At high strain rate, the HY100 steel thermally softened more than the other two steels. The effect of temperature on failure strain is less pronounced under high strain rate loading. A 37% reduction of failure strain in HY100, 20% in HY130, and almost no reduction in AF1410 steel was observed.

**a. Strain Hardening**

Figure 7 compares the stress-strain curves from the high temperature QS and SHB tests for the three steels. The onset of plastic instability in all the high temperature tests precluded the possibility of evaluating the strain hardening behaviors under elevated temperatures. The negative slopes of the stress-strain curves at low (QS) and high (SHB) strain rate loading conditions are very similar for each steel, indicating similar necking evolution characteristics.

**b. Failure Strain**

At elevated temperatures, the strain at failure was substantially higher in the SHB tests than in the QS tests. HY100 exhibited about 40% higher failure strain, while HY130 and AF1410 exhibited 60% and 100% higher failure strains, respectively. In general, the ductility in the three steels decreased at high temperature (400°C), irrespective of the strain rates. The microstructural evaluations of the fractured specimens from both QS and SHB tests did not lead to any definite finding to explain the reduction in ductility at high temperature. We can only speculate that the ductility decreased due to the combined effects of early occurrence of the onset of plastic instability (necking) and adiabatic heating.

**c. Strain Rate Hardening**

A comparison of high temperature stress-strain curves between the low (QS) and high (SHB) strain rates is made in Figure 7 for the three steels. The HY100 steel exhibited a similar level of rate sensitivity at both room and high temperatures. The HY130 and AF1410 steels, which did not exhibit any strain rate dependency at room temperature, exhibited significant rate hardening at 400°C. In fact, the rate sensitivity in AF1410 at 400°C was much higher compared to the rate sensitivity in HY100 and HY130.

Figure 8 summarizes the effects of temperature on strain rate hardening in the three steels. The slopes of the lines indicate the levels of strain rate sensitivity. For HY100, the slopes for 23°C and 400°C are very similar, indicating minimal effect of temperature on the strain rate hardening behavior of this steel. The HY130 and AF1410 steels both showed increased rate sensitivity at high temperature. This temperature effect was more significant in AF1410, as indicated by the slopes of the lines in Figure 8.

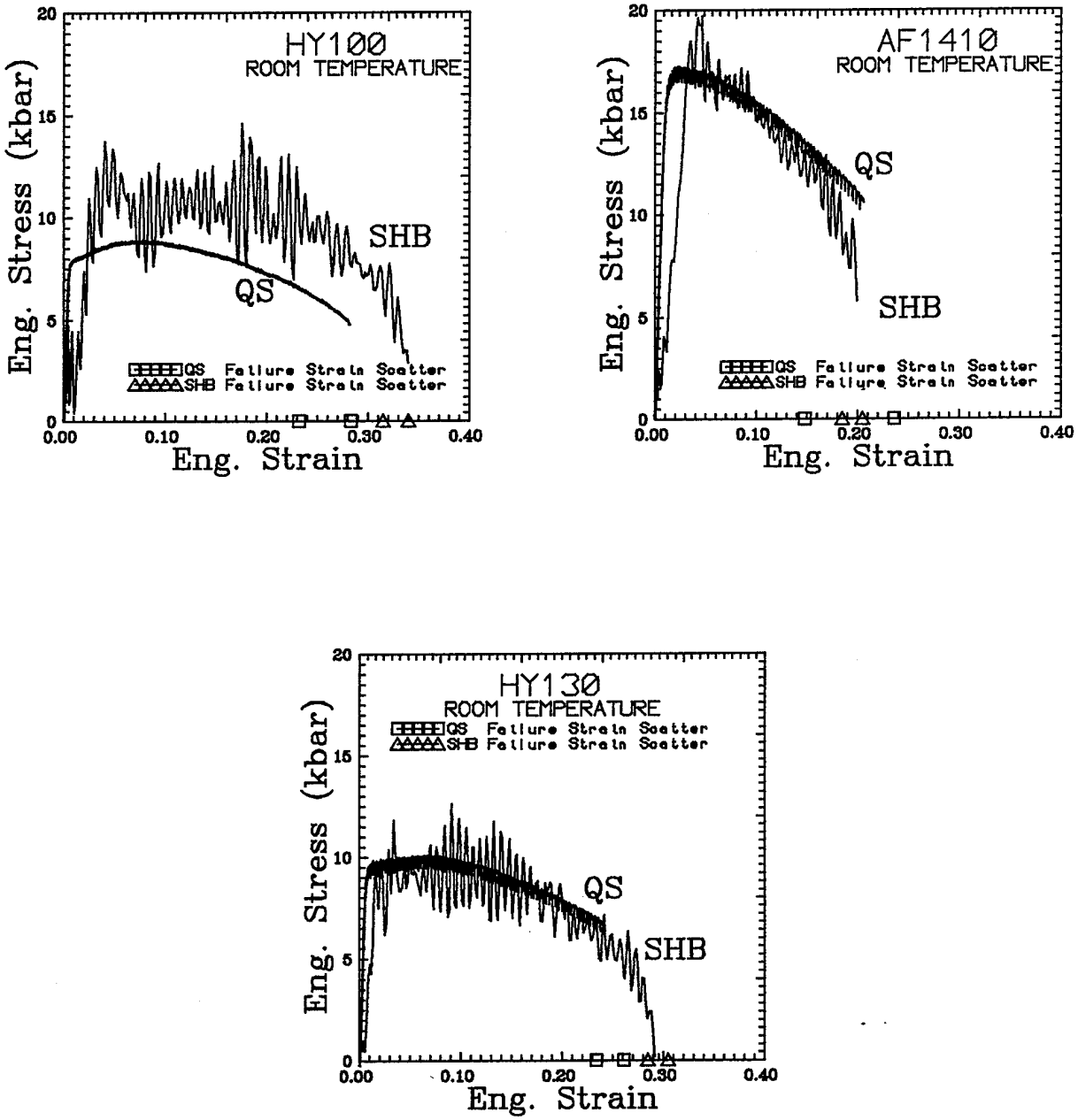


Figure 4. Effect of strain rate on stress-strain behavior of HY100, AF1410, and HY130 steels at room temperature.

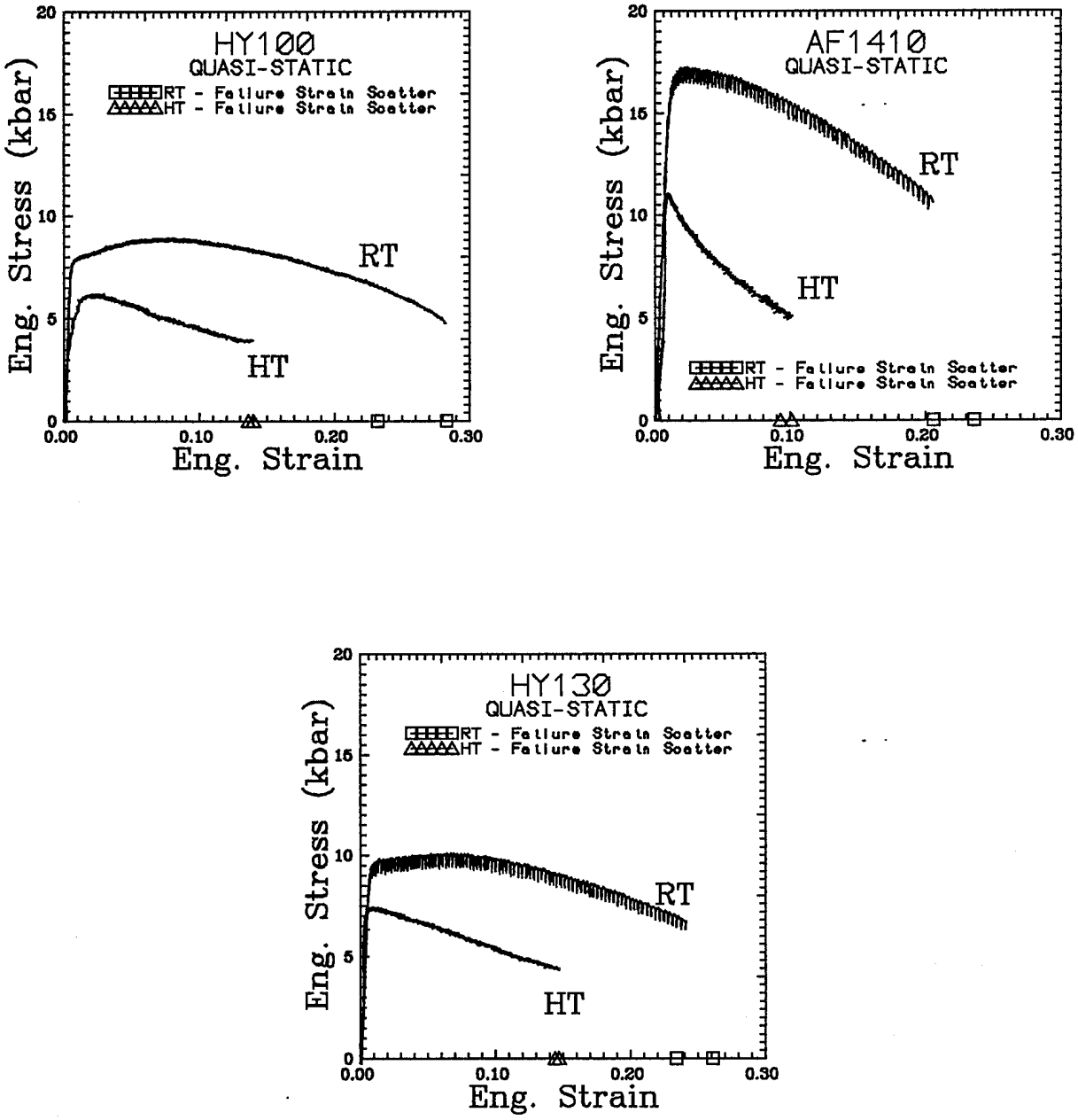


Figure 5. Effect of temperature on quasi-static stress-strain behaviors of HY100, AF1410, and HY130 steels at room and high (400°C) temperatures.

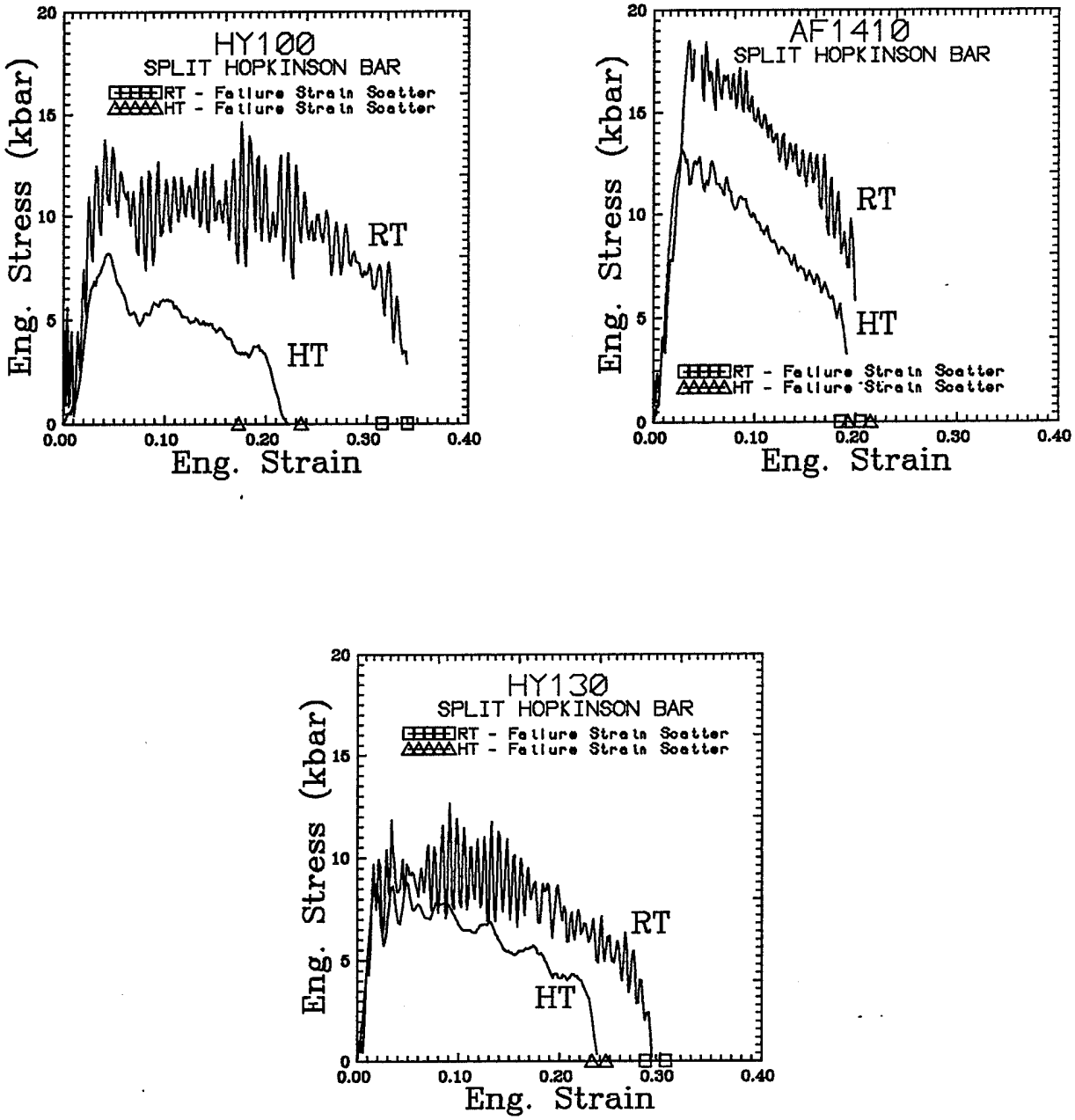


Figure 6. Effect of temperature on dynamic (SHB) stress-strain behaviors of HY100, AF1410, and HY130 steels at room and high (400°C) temperatures.

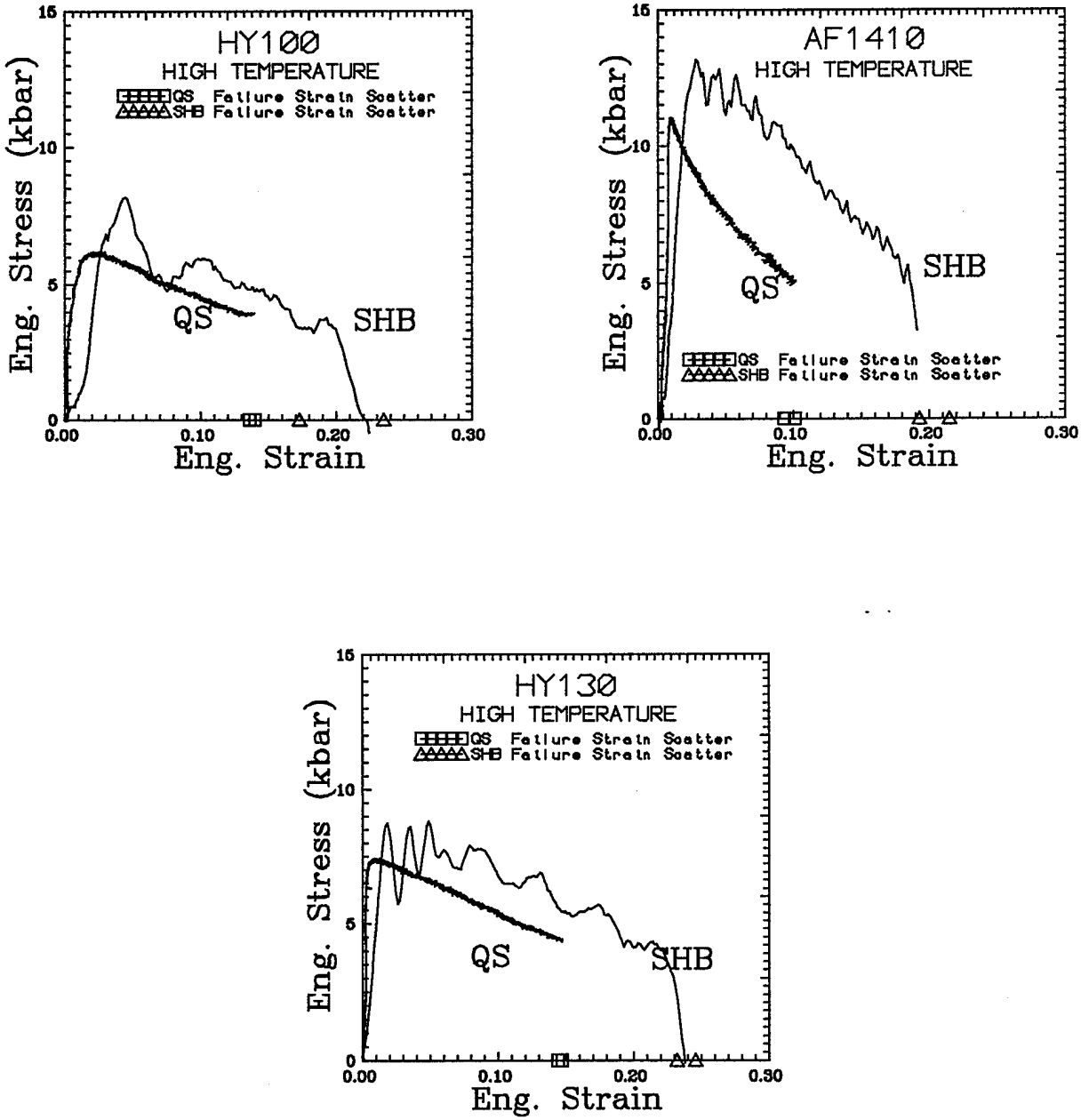


Figure 7. Effect of strain rate on stress-strain behaviors of HY100, AF1410, and HY130 steels at high (400°C) temperature.

Finally, the effects of strain rate on thermal softening are shown in Figure 9. The rate of thermal softening is consistently higher at lower strain rate (0.001/s) for all three steels. For HY100, the slopes for 0.001/s and 1450/s are almost same, indicating that the thermal softening in this steel is relatively insensitive to the strain rate. The flow stress in AF1410 steel rapidly decreased with respect to temperature at a strain rate of 0.001/s. This steel exhibited the most significant influence of strain rate on thermal softening. The thermal softening in HY130 was not very sensitive to the strain rate.

### 4.3 Bridgman Analysis of Necking

The uniaxial stress-strain data obtained from conventional quasi-static and SHB tests are not valid beyond the onset of necking, due to the development of localized deformation and a triaxial state of stress. Bridgman's [13] analysis provides a method to obtain the effective stress and strain from the measurement of the neck profile. In this study, a Bridgman analysis was successfully employed to obtain stress-strain data beyond necking.

In the Bridgman analysis, the effective plastic strain is given by,

$$\epsilon^{P}_{eff} = -2\ln\left(\frac{d}{d_o}\right) \tag{2}$$

where d is the current diameter of the neck and $d_o$ is the original diameter of the specimen. The effective stress, $\sigma_{eff}$, is related to the true stress, $\sigma_t$, (which is equal to the load divided by the current cross-sectional area), by the following relation,

$$\sigma_{eff} = B\sigma_t \tag{3}$$

and the correction factor B is given by,

$$B = \frac{1}{\left(1+\frac{2R}{a}\right)\ln\left(1+\frac{a}{2R}\right)} \tag{4}$$

where a is the current neck radius and R is the current radius of curvature of the neck profile. A high-speed camera with a framing rate of 100,000 frames/sec is used to obtain photographs of the necking specimen every 10 microseconds.

In this study, the Bridgman analysis was performed on one SHB tensile test at room temperature for each steel. The high speed photographs of the development of the neck profile during the SHB tensile test are shown in Figures 10, 11, and 12 for AF1410, HY100, and HY130, respectively. In these figures, the uniform strain values away from the necked regions are also shown for each frame at an interval of 10 microseconds. The Bridgman parameter B was determined from the measured values of a, d and R from the photographs of each frame. The equations mentioned above are then used to calculate the stress and strain beyond necking.

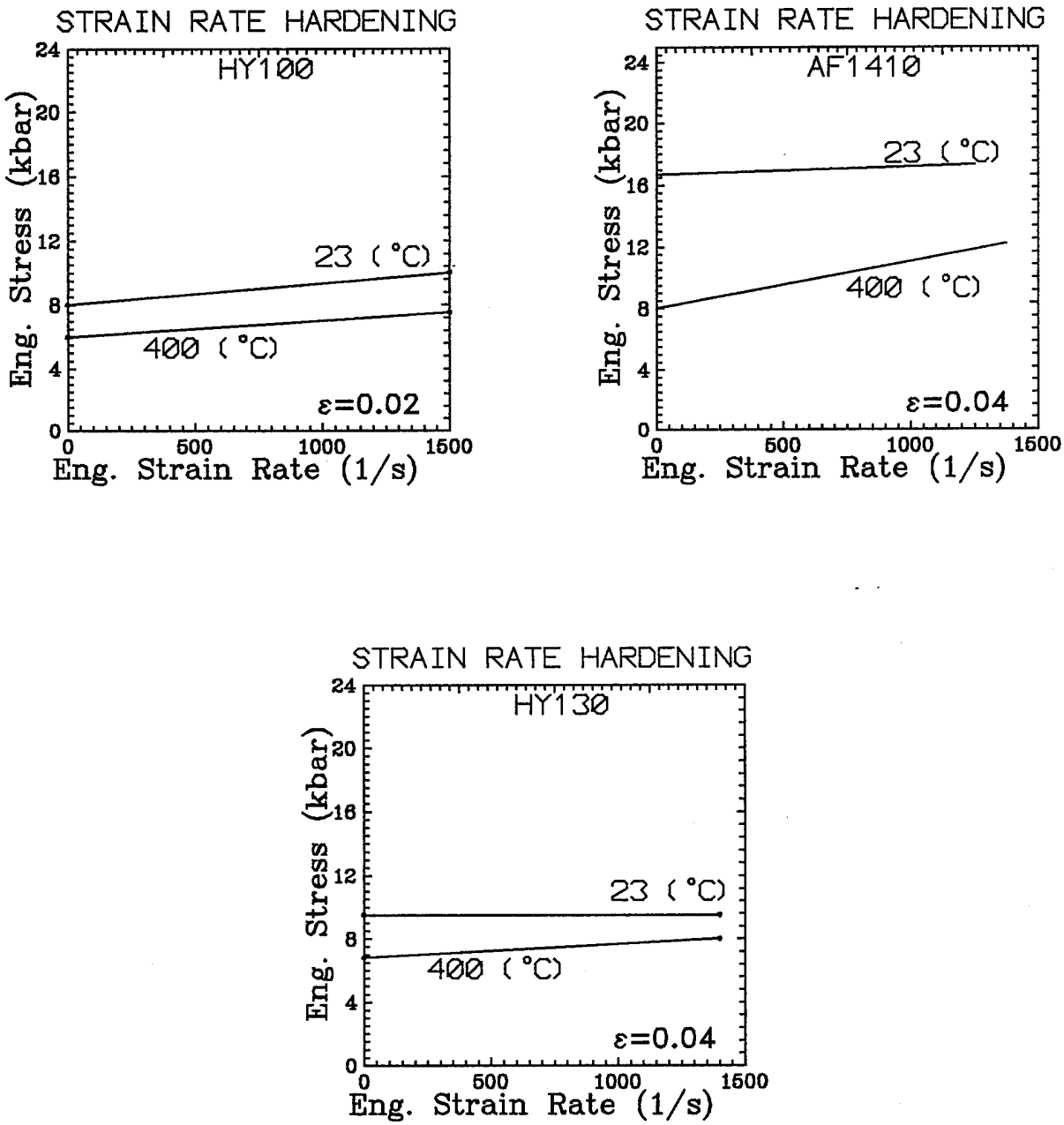


Figure 8. Effect of temperature on strain rate sensitivity (slope of the lines) in HY100, AF1410, and HY130 steels.

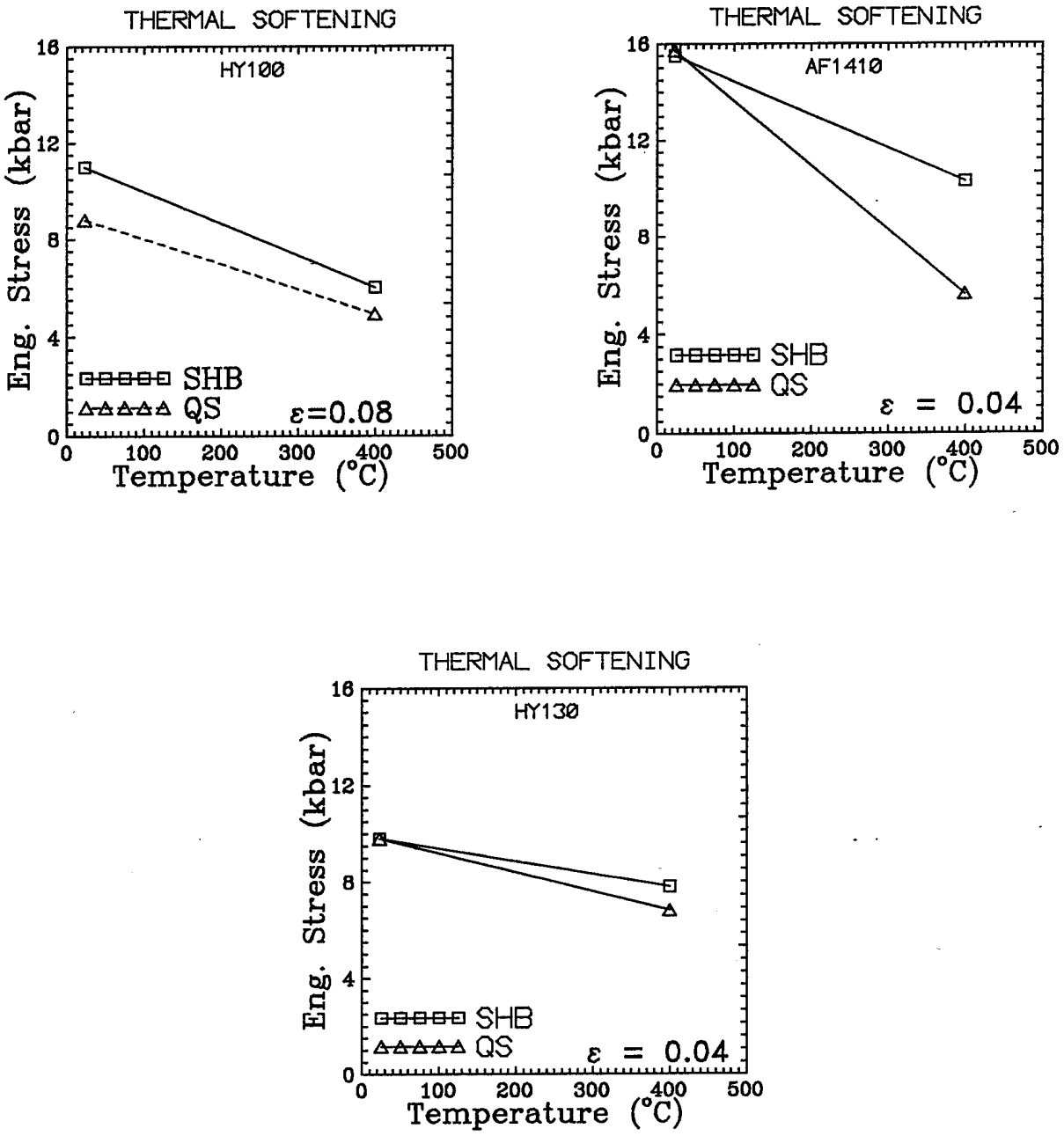


Figure 9. Effect of strain rate on thermal softening behavior of HY100, AF1410, and HY130 steels.

It was observed that the development of necking begins very early in the AF1410 alloy (at about 65 μsec) at a true strain of 0.061 (frame #5 in Figure 10), while it is much delayed in the HY100 alloy, initiating at about 164 μsec at a true strain of 0.204 (frame #4 in Figure 11). The HY130 alloy shows an intermediate behavior in which necking begins to develop at about 111 μsec at a true strain of 0.121 (frame #3 in Figure 12). The stress-strain curves for the SHB room temperature tests shown earlier in Figure 6 support these observations from the high speed photographs.

It has been observed by previous investigators [13,15] that the development of a neck profile geometry is similar for many metals. In particular, the relationship between the neck radius of curvature, R, and the neck radius, a, shows similar behavior for different metal alloys.

In Figure 13, the neck radius, a, is plotted versus the neck radius of curvature, R, (both scaled by the original radius of the specimen, $a_o$ ) for the three different alloys. It can be seen that all three alloys show more or less the same necking behavior. The effective stress-strain curves obtained from the Bridgman analyses of the above SHB tests on AF1410, HY100 and HY130 alloys are shown in Figure 14. For the AF1410 and HY100 alloys, the data points seem to fit a power law relation, while for the HY130 alloy, the data points appear to fit an exponential relation. The effective stress - effective plastic strain curve for HY130, constructed using the neck profile data, exhibited a significantly higher peak flow stress than the curves for HY100 and AF1410 steels.

### 4.4 Fracture Analysis

The results and discussion presented in this section focus on the features of the fracture surfaces of each steel tested under each loading condition: 1) QS (0.001/sec) at RT, 2) QS at 400°C, 3) SHB (1500/sec) at RT, and 4) SHB at 400°C. These features may lend insight into the relative contribution to failure of microvoid formation, growth and coalescence. This information is important to the material failure modeling effort. The majority of dynamic failure models for metals focus on damage accumulation. This damage accumulation is based on the nucleation, growth and coalescence of voids. A ductile fracture surface is characterized by a dimpled surface resulting from microvoid nucleation, growth and coalescence. The microvoids usually originate at second phase particles within the necked region. The three steels exhibited ductile failure when tested in tension under several testing conditions. The strength and the failure characteristics of these tempered martensitic steels are controlled by a combination of microstructural components including: (1) martensitic packet size (2) presence of carbides controlled by heat treatment (e.g. $Fe_3C$) and (3) presence of other nonmetallic particles (e.g. MnS) due to processing [7].

#### a. HY100

In Figures 15 and 16, micrographs of the fracture surfaces of HY100 tested under the four conditions are presented. These micrographs of the fracture surfaces are obtained from the scanning electron microscope (SEM). The SEM micrographs, taken at low magnification (~50X), are presented in Figure 15. Each micrograph was taken looking onto the fracture surface along the tensile axis. From the overall fracture surface appearance, it is evident that HY100 exhibited ductile failure when tested under each combination of strain rate and temperature included in this study. Each fracture surface exhibits a central fibrous region. The outer smooth region is the shear lip region where fast fracture occurred. These types of features are typical of a ductile tensile fracture surface on a round cylindrical specimen [17]. Presented in Figure 16 are higher magnification (~300X) micrographs of the central fibrous region of each sample presented in Figure 15.

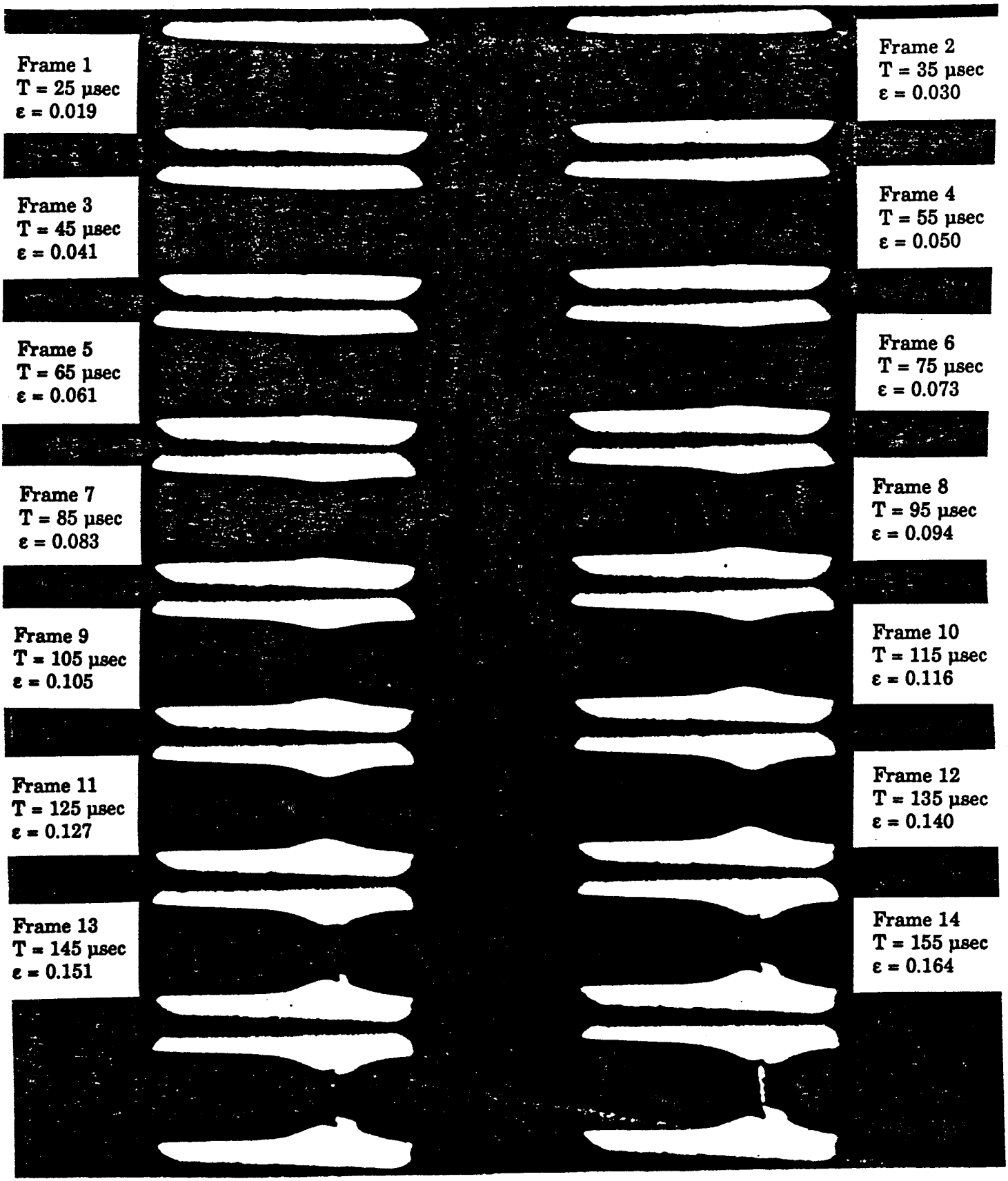


Figure 10. High speed photographs of necking evolution in AF1410 (SHB) tensile sample.

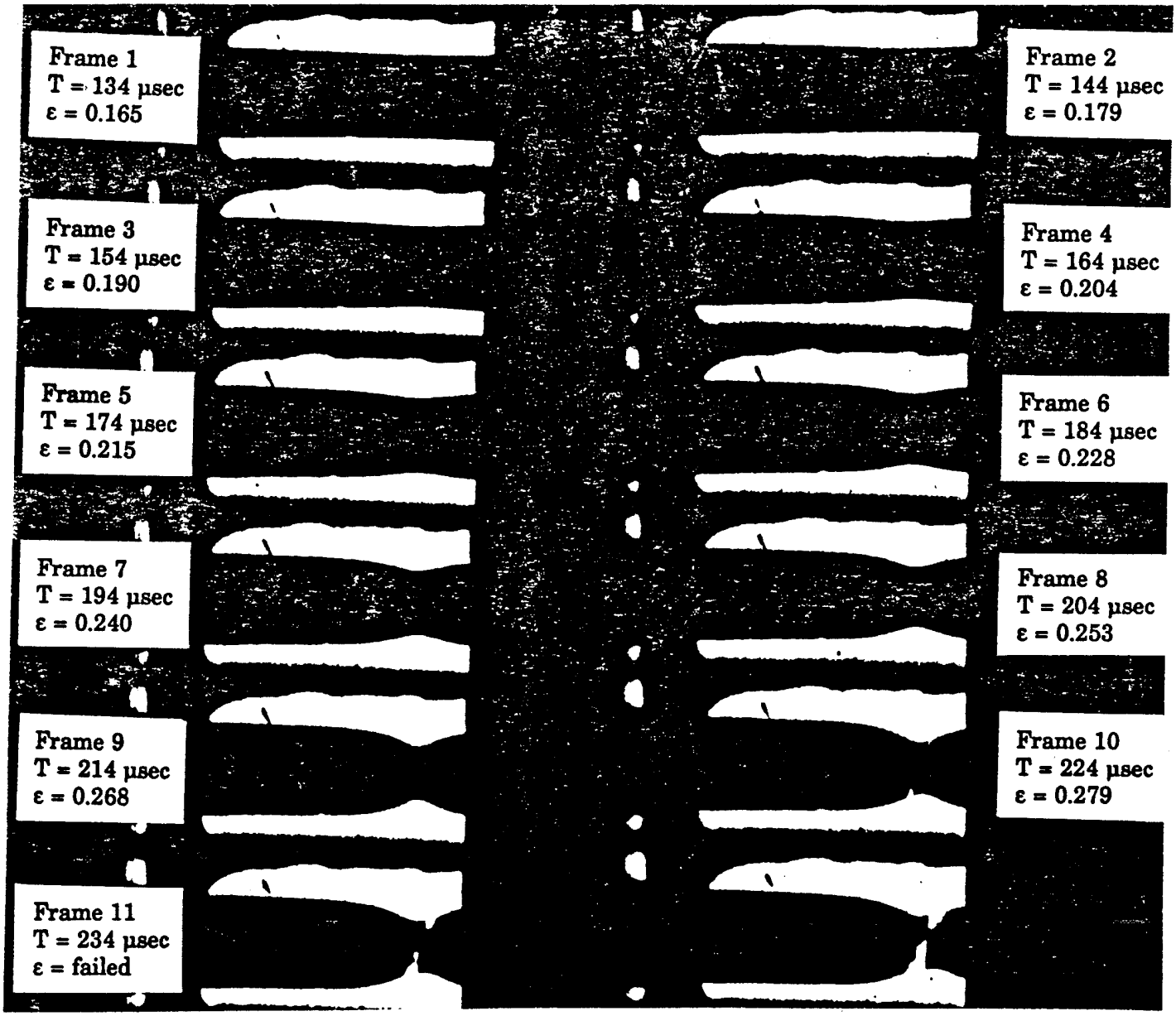


Figure 11. High speed photographs of necking evolution in HY100 (SHB) tensile sample.

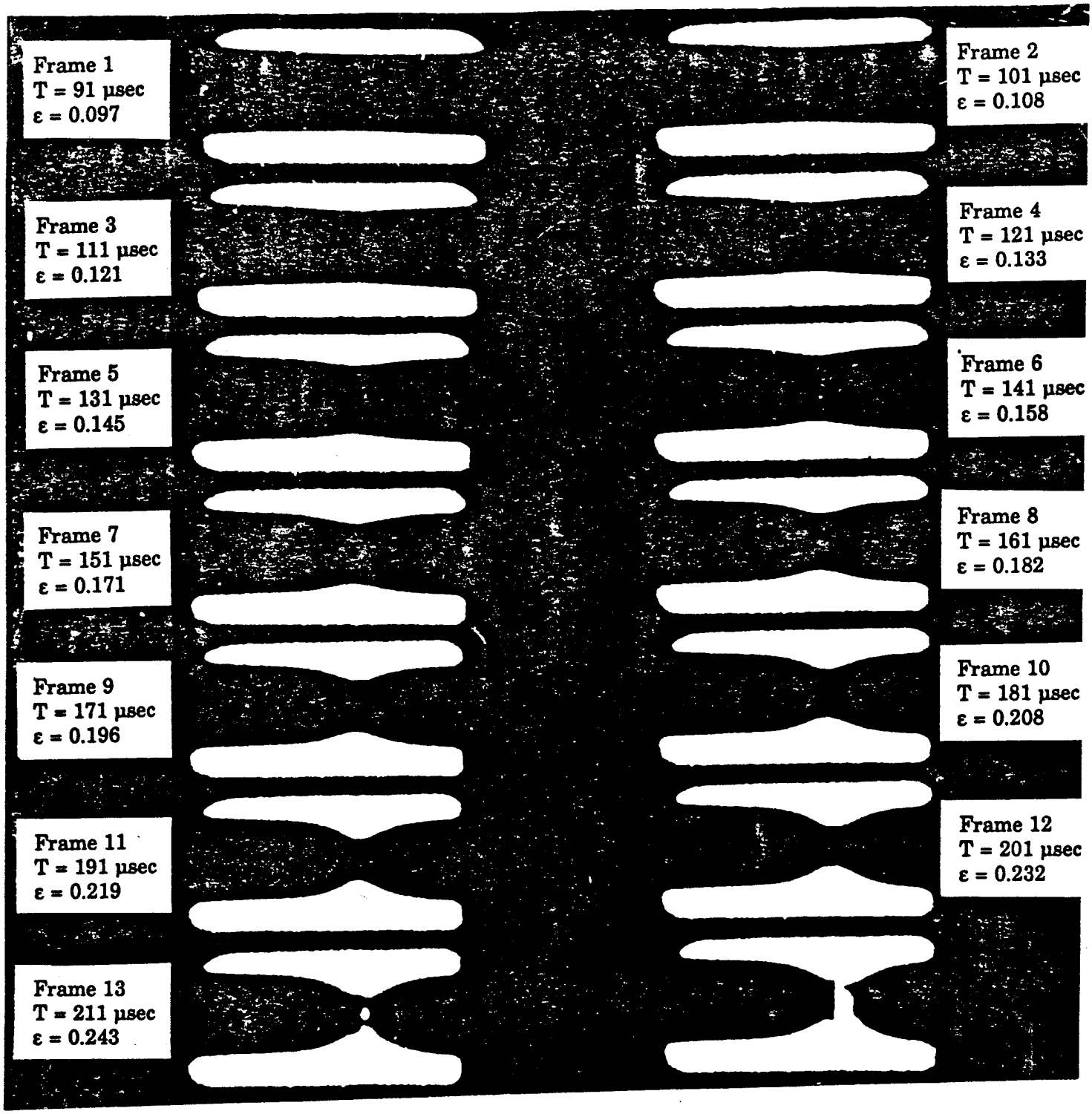


Figure 12. High speed photographs of necking evolution in HY130 (SHB) tensile sample.

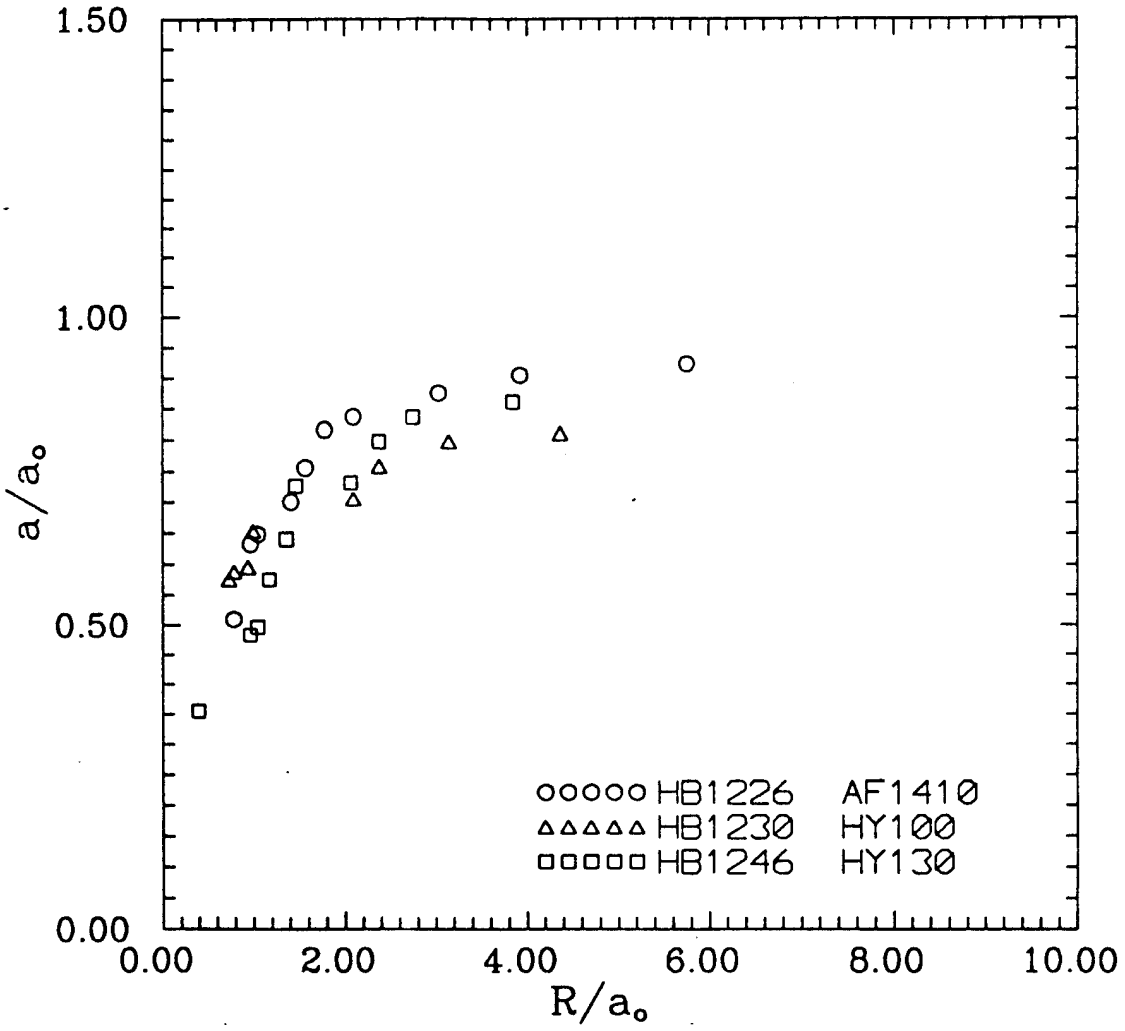


Figure 13. The variation of minimum radius (a) of the neck with respect to the radius of curvature (R) of the neck profile for HY100, HY130, and AF1410 steels. $a_0$ is the initial uniform radius of the specimen.

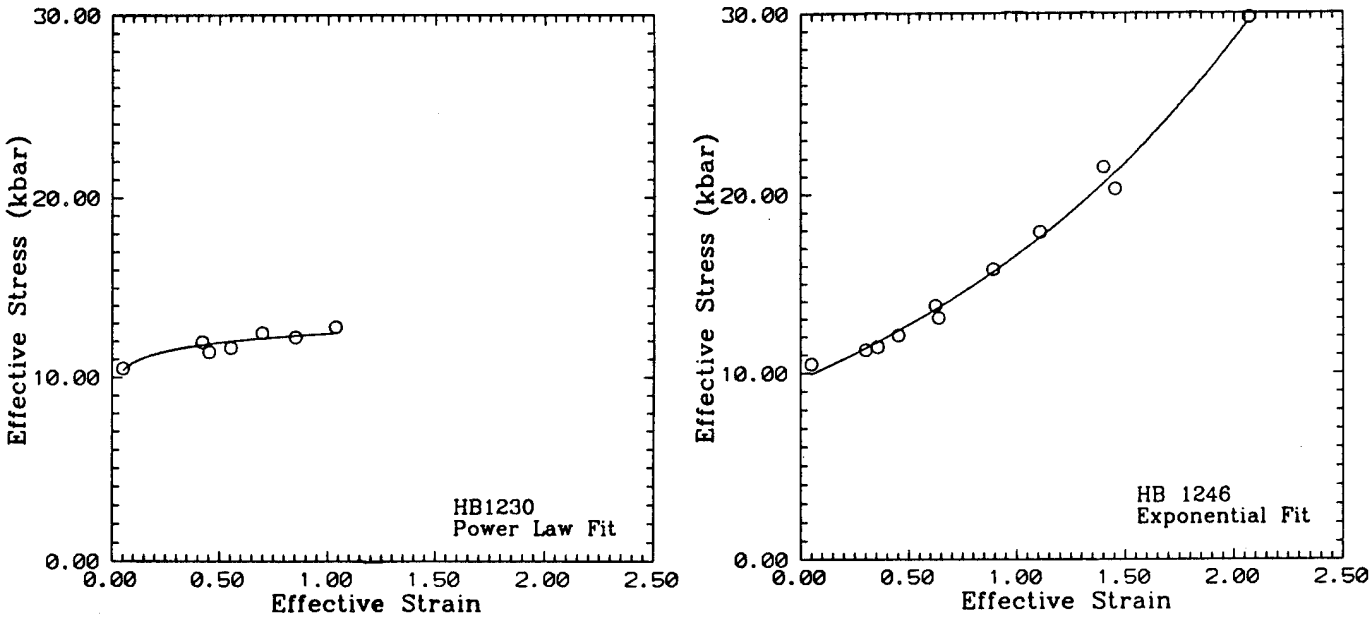


(a) (b)

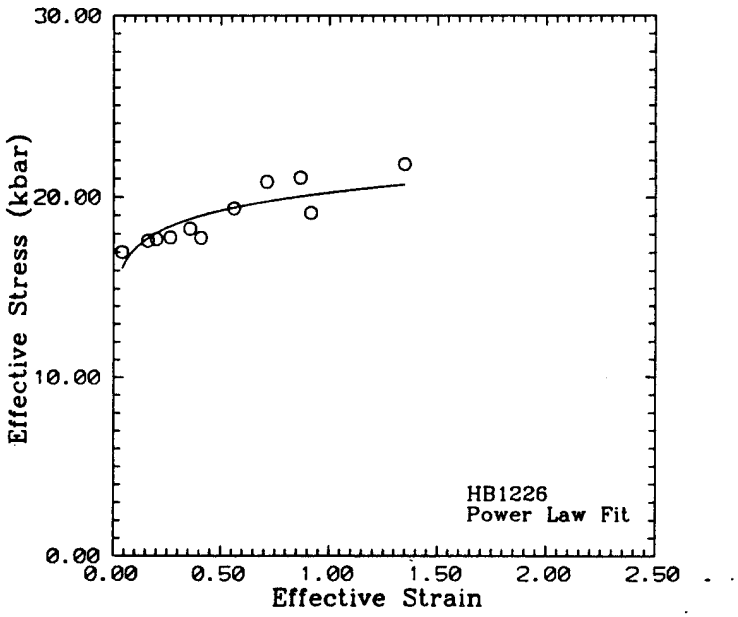


(c)

Figure 14. Effective stress versus effective plastic strain constructed using the Bridgman analyses of the high speed photographs of the necking tensile samples: (a) HY100, (b) HY130, and (c) AF1410.

In all samples, this fibrous region is dimpled. This dimpled surface appearance is attributed to microvoid nucleation, growth and coalescence occurring within the necked region of a tensile sample [17]. Even though each of these HY100 samples was tested under different conditions, the fracture surfaces are similar. This observation indicates that the manner in which damage accumulated and fracture occurred for each test condition is similar. The relative contribution of microvoid formation, growth and coalescence to the overall fracture is similar in each sample. Consequently, one material model describing damage accumulation for the range of test conditions employed should be sufficient.

**b. HY130**

Presented in Figures 17 and 18 are SEM micrographs of HY130 samples tested under each combination of temperature and strain rate included in this study. Consistent with a ductile tensile fracture, the fracture surface of each sample has a central fibrous region and an outer shear lip region (see Figure 17). However, there are some apparent differences between the various fracture surfaces. A micrograph of the fracture surface of an HY130 specimen tested at a strain rate of 0.001 $sec^{-1}$ at a temperature of 24°C is presented in Figure 17a. Unlike the other HY130 fracture surfaces, radial cracks are observed within the central fibrous region.

The radial cracks usually point to the initiation site of the fracture. In this case the cracks point towards the center of the sample where the microvoids first formed at an earlier stage of the fracture process. Fracture in the region containing the radial cracks is usually a mixture of dimple rupture and cleavage. A micrograph of the fracture surface of an HY130 specimen tested at a strain rate of 1400 $sec^{-1}$ at a temperature of 400°C is presented in Figure 17d.

It is observed that the shear lip region is extensive compared to the other HY130 fracture surfaces. There are also voids present within the shear lip region near the central fibrous region. This observation indicates that voids formed throughout the necked region. The formation, growth and coalescence of the voids at the center of the specimen resulted in tensile overload. The shear lip formed at the outer region due to this overload prior to the coalescence of the voids already present in the outer region.

The higher magnification (~300X) micrographs of the central fibrous region are shown in Figure 18. The dimpled appearance of each fracture surface is similar for each HY130 sample, irrespective of the test conditions. These microdamage features of voids indicate that a material failure model based on ductile void growth should be applicable over the range of test conditions employed in the present study.

**c. AF1410**

The SEM micrographs of AF1410 specimens tested under each combination of temperature and strain rate are shown in Figure 19, 20 and 21. The fracture surfaces of the sample tested at 0.001 $sec^{-1}$ at a temperature of 24°C and both samples tested at higher strain rates (1300 to 1350 $sec^{-1}$ at 24°C and 400°C) have a similar appearance, as indicated by Figures 19a, 19c and 19d. All these samples have central fibrous zones and outer shear lip regions of similar size. However, unlike the other AF1410 fracture surfaces, radial cracks are observed within the central fibrous region of the sample tested at 0.001 $sec^{-1}$ and 24°C (Figure 19a). The fracture surface of the specimen tested at 0.001 $sec^{-1}$ at a temperature of 400°C (Figure 19b) has only a central fibrous region with no extensive shear lip observed.

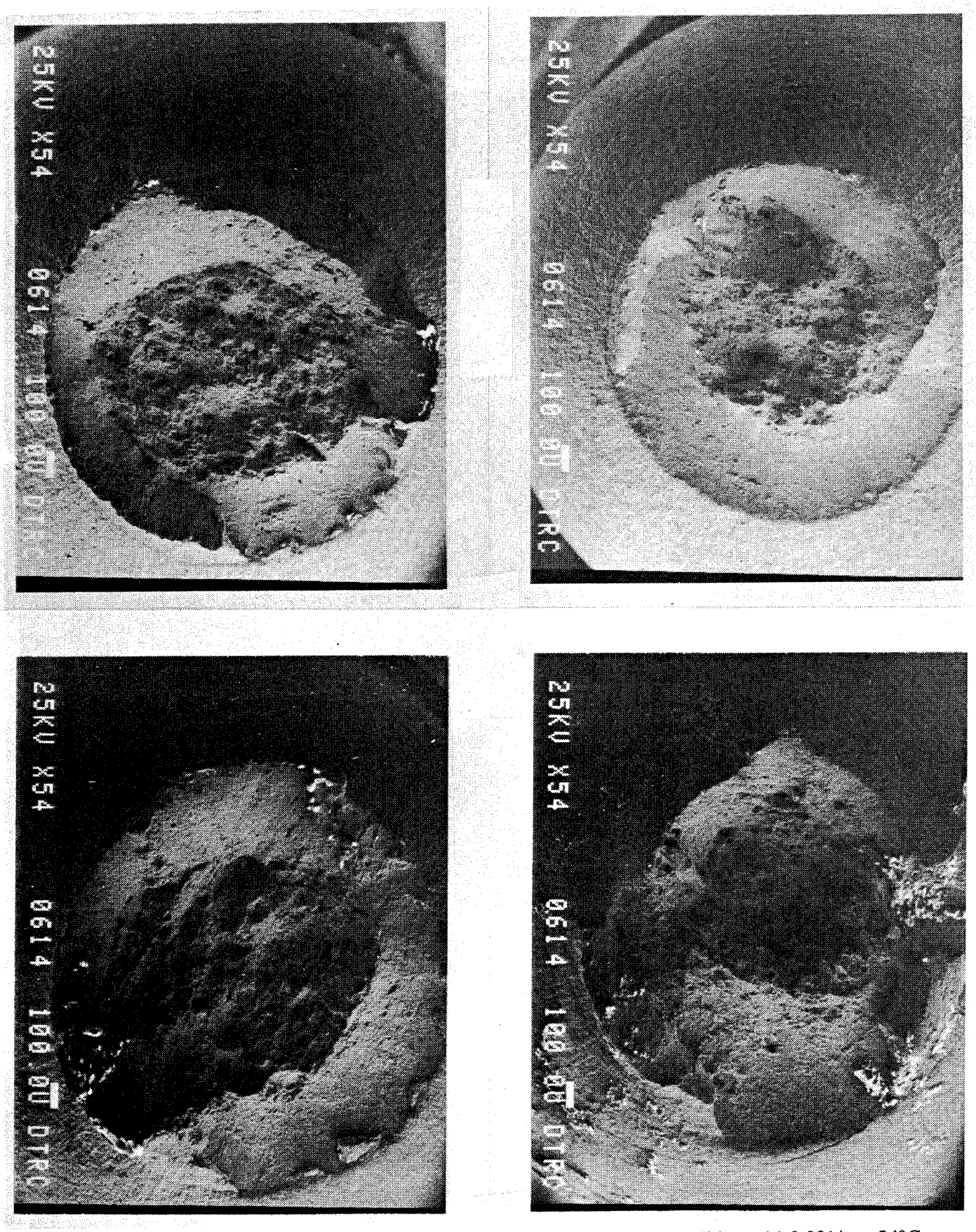


Figure 15: SEM micrographs of HY100 tensile fracture surfaces. Test conditions: (a) 0.001/sec, 24°C (b) 0.001/sec, 400°C (c) 1500/sec, 24°C (d) 1500/sec, 400°C.

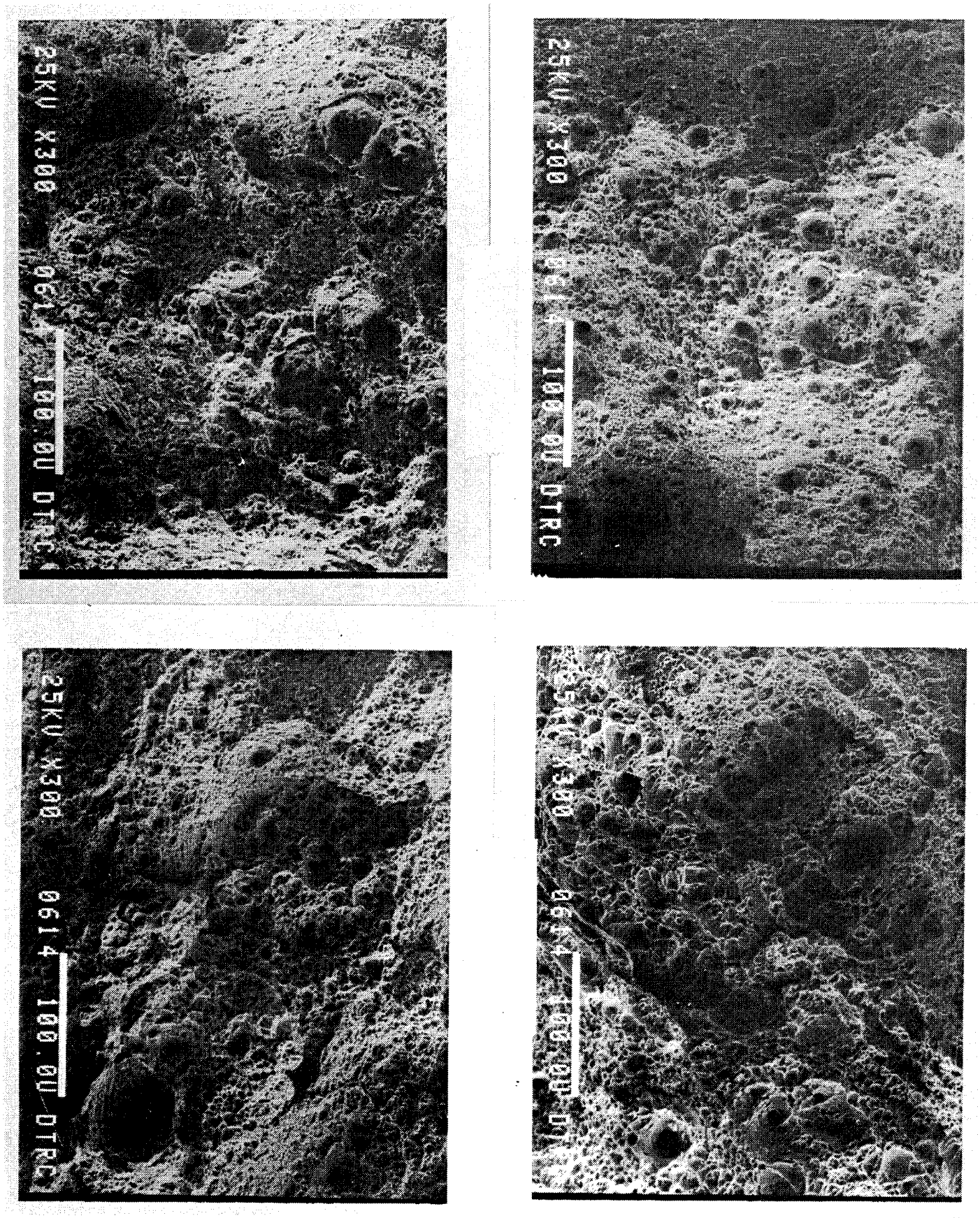


Figure 16: SEM micrographs of HY100 tensile fracture surfaces. Test conditions: (a) 0.001/sec, 24°C (b) 0.001/sec, 400°C (c) 1500/sec, 24°C (d) 1500/sec, 400°C.

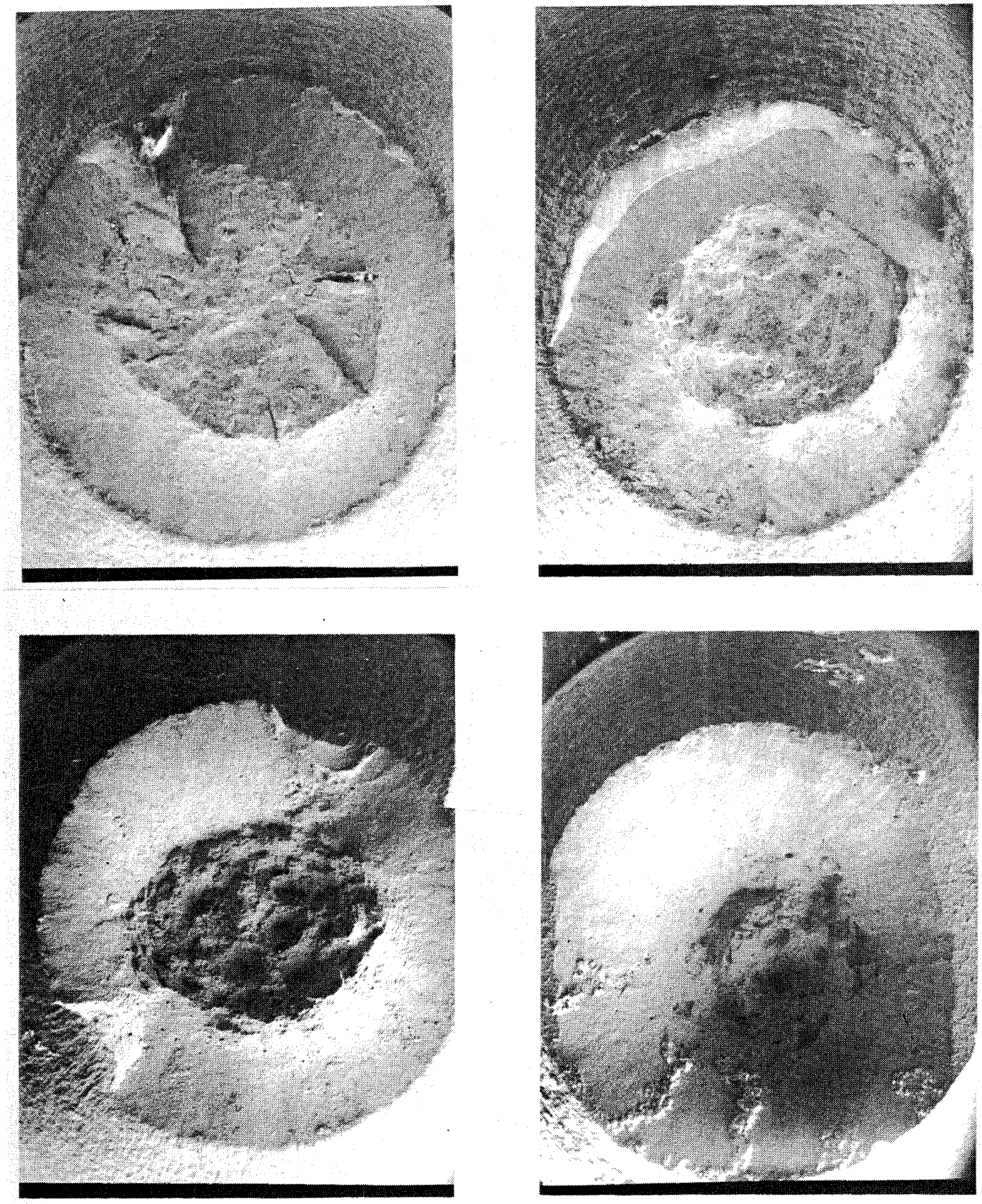

Figure 17: SEM micrographs of HY130 tensile fracture surfaces. Test conditions: (a) 0.001/sec, 24°C (b) 0.001/sec, 400°C (c) 1400/sec, 24°C (d) 1400/sec, 400°C.

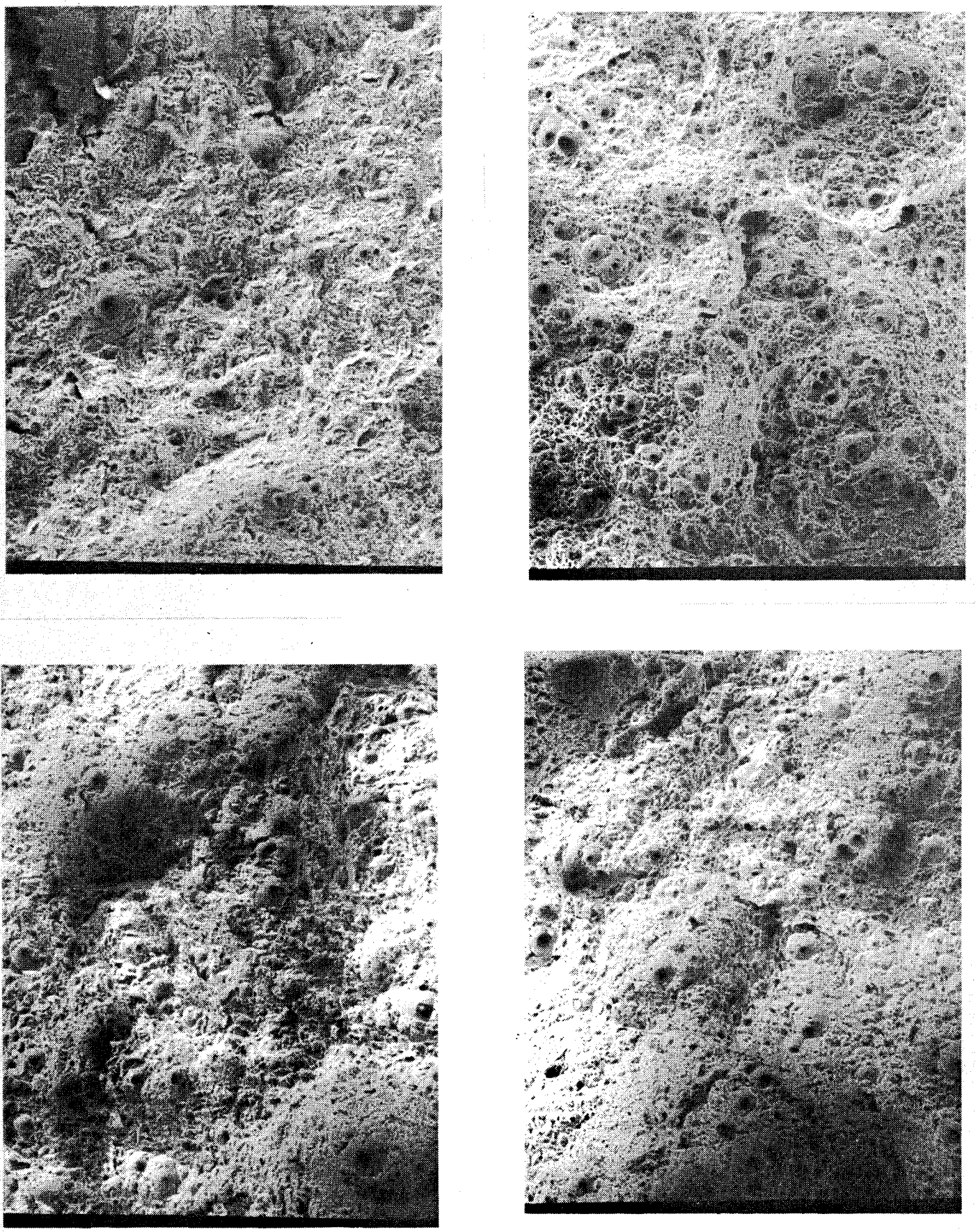

Figure 18: SEM micrographs of HY130 tensile fracture surfaces. Test conditions: (a) 0.001/sec, 24°C (b) 0.001/sec, 400°C (c) 1400/sec, 24°C (d) 1400/sec, 400°C.

The fracture surfaces of the samples shown at a lower magnification in Figure 19 are repeated in Figure 20 at a higher magnification (~300X) for further evaluation. Each fracture surface has a different appearance. A micrograph of the specimen tested at a strain rate of 0.001 $sec^{-1}$ at a temperature of 24°C is presented in Figure 20a. The surface contains voids having a wide range in size. It appears that the coalescence of the larger voids occurred by formation, growth and coalescence of voids within the remaining metal ligaments between the larger voids. This is not the case for the specimen tested at a strain rate of 0.001 $sec^{-1}$ at a temperature of 400°C presented in Figure 20b. Compared to Figure 20a, the voids are larger and lie within a narrower size range. This indicates that the voids coalesced due to void growth and shear of the remaining ligaments between the voids rather than by nucleating voids within the remaining metal ligaments.

A micrograph of the specimen tested at a strain rate of 1300 $sec^{-1}$ at a temperature of 24°C is presented in Figure 20c. The fracture surface contains voids having a wide range in size. This observation is similar to that of the specimen tested at the same temperature but lower strain rate, Figure 20a. However, it appears that when the AF1410 was tested at the higher strain rate, the smaller voids in the ligaments between the larger voids are well developed compared to the smaller voids in the specimen tested at the same temperature but lower strain rate (see Figure 21a and 21b). A micrograph of the specimen tested at a strain rate of 1350 $sec^{-1}$ at a temperature of 400°C is presented in Figure 20d. The fracture surface contains voids having a wide range in size. The larger voids appear to have undergone more growth compared to the larger voids in the sample tested at the same strain rate but lower temperature (Figure 20c). Also, the smaller voids in ligaments adjoining the larger voids are well developed compared to the other two samples where a wide range in void sizes was noted (Figure 21).

The above observations indicate that the relative contribution of microvoid formation, growth and coalescence to the fracture of AF1410 differs depending on temperature and strain rate. The damage accumulation in AF1410 appears dependent on test conditions (i.e. temperature and strain rate).

**d. Plate Impact Samples**

Microscopic evaluation of the spalled target plates further confirmed that the failure of the three steels under shock loading conditions is due to microvoid nucleation, growth and coalescence. Optical photomicrographs of the spall areas in the 8 mm thick target plates are shown in Figures 22, 23, and 24. Void nucleation and growth occurred at regions around the main spall plane which was located at a distance of 3 mm from the target's back surface. HY100 and AF1410 steels exhibited intense void formation, nucleation and growth, along several parallel spall planes.

Optical photomicrographs of an 8 mm thick HY100 target plate etched with 1% nital exhibit localized deformation bands that appear to be adiabatic shear bands, Figure 25. These bands are in the regions where spallation has occurred. The center of the band appears to have etched "white". This would indicate that the band was of the transformed type [18]. Presented in Figure 26 are SEM micrographs of the same HY100 target plate. The shear band is narrow (< 10μm). The higher magnification micrographs in Figure 26 clearly show that the voids formed are joined by a shear band. These results indicate that shear bands may form as a result of the combination of microvoid formation, test condition and loading history. The connection between the bands and the voids indicates that the formation of the shear band may occur after the voids have formed and may act as a means by which the voids join. This would be similar to the observation of void sheeting within localized bands observed for ductile materials that were tested in tension. Further work is needed to determine a correlation among the shear bands, microvoids, loading history and test conditions for this steel.

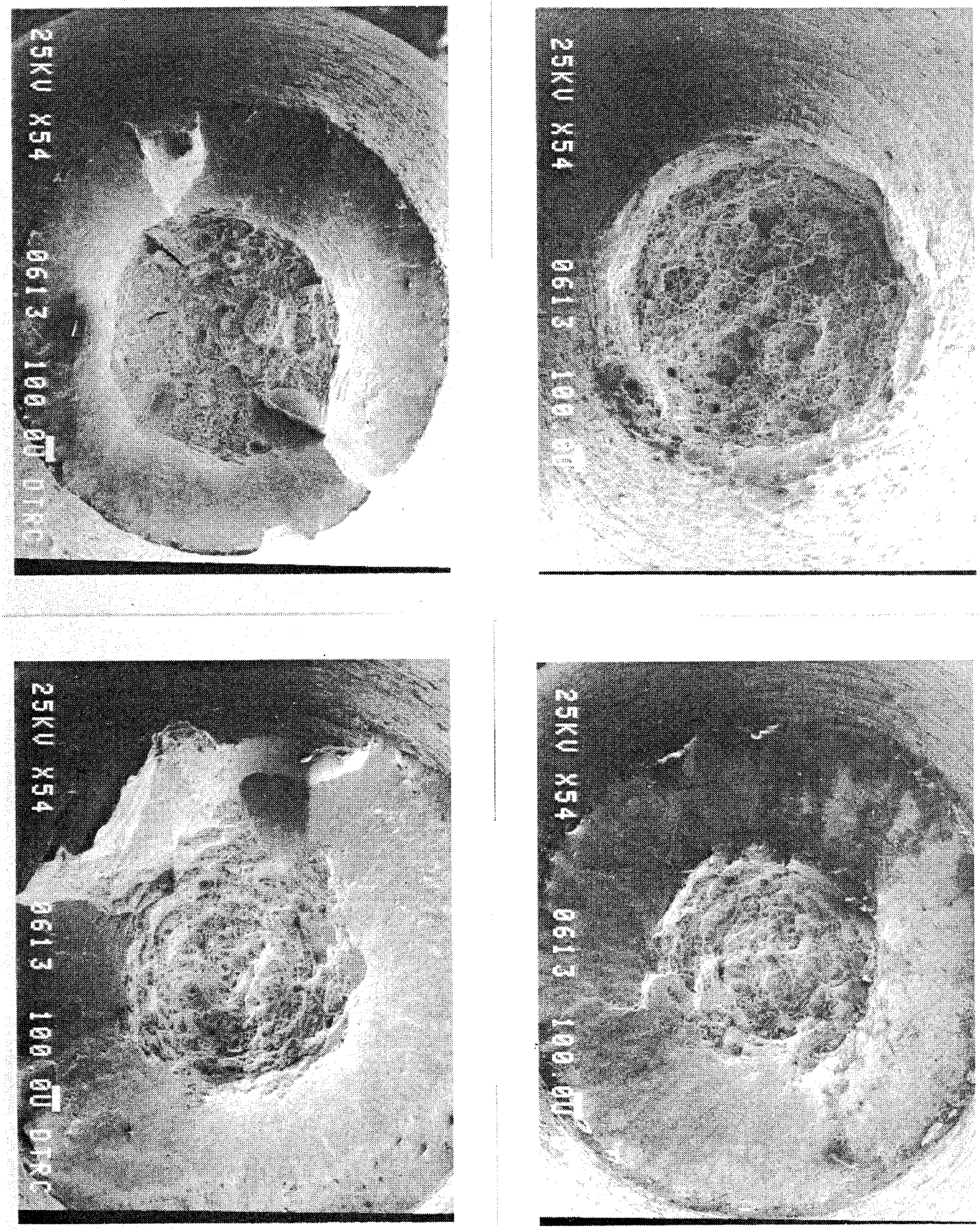


Figure 19: SEM micrographs of AF1410 tensile fracture surfaces. Test conditions: (a) 0.001/sec, 24°C (b) 0.001/sec, 400°C (c) 1300/sec, 24°C (d) 1350/sec, 400°C.

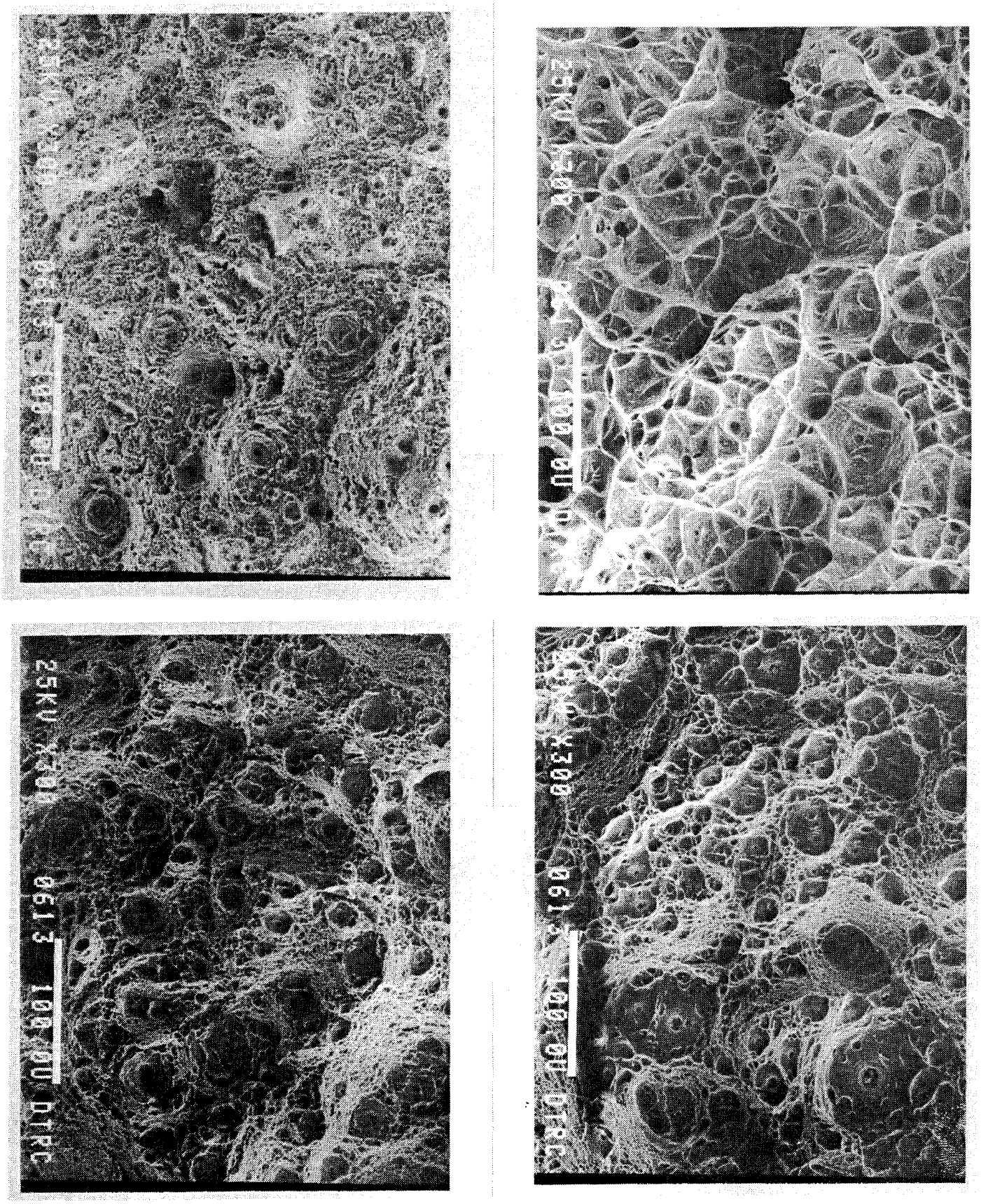

Figure 20: SEM micrographs of AF1410 tensile fracture surfaces. Test conditions: (a) 0.001/sec, 24°C (b) 0.001/sec, 400°C (c) 1300/sec, 24°C (d) 1350/sec, 400°C.

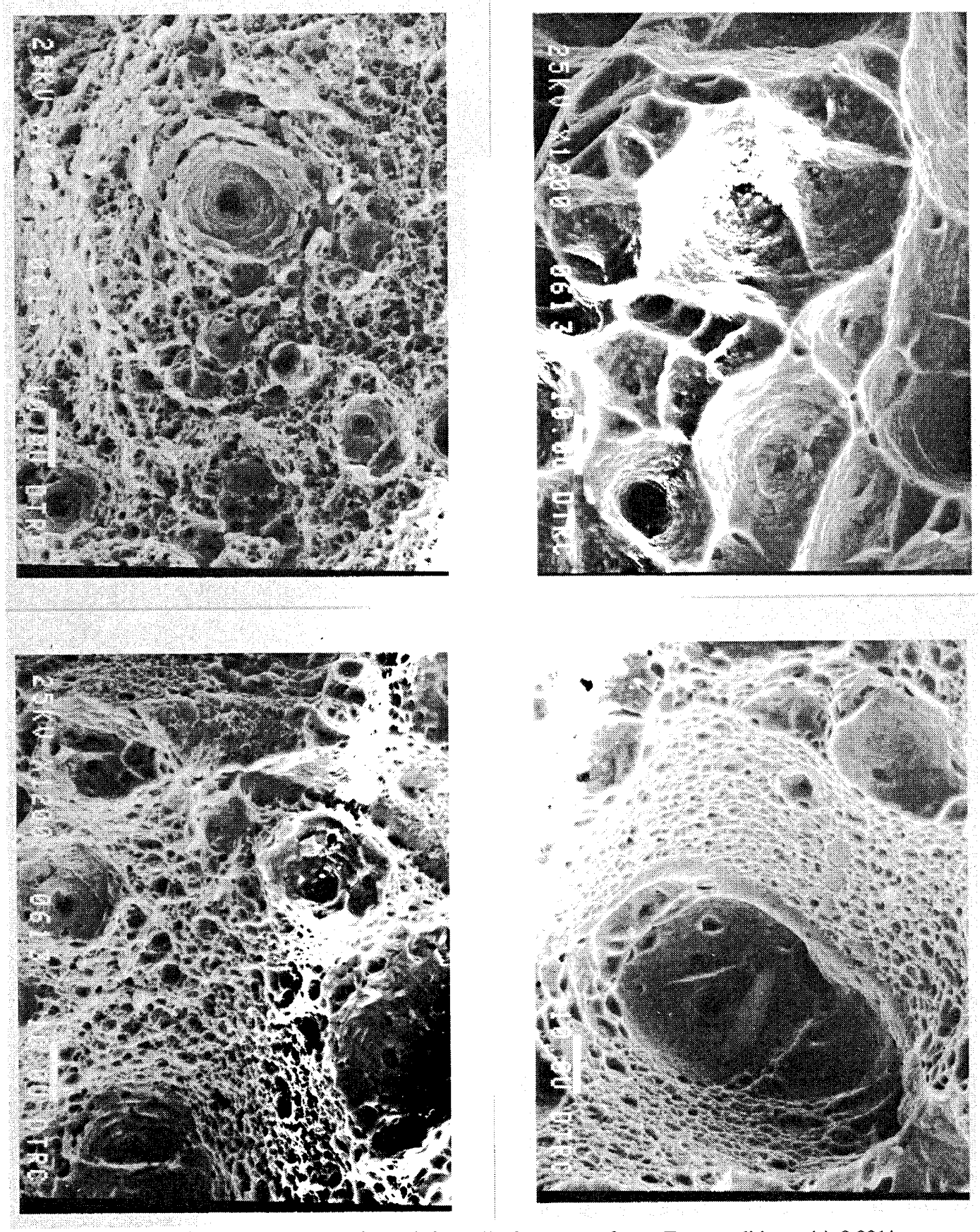

Figure 21: SEM micrographs of AF1410 tensile fracture surfaces. Test conditions: (a) 0.001/sec, 24°C (b) 0.001/sec, 400°C (c) 1300/sec, 24°C (d) 1350/sec, 400°C.

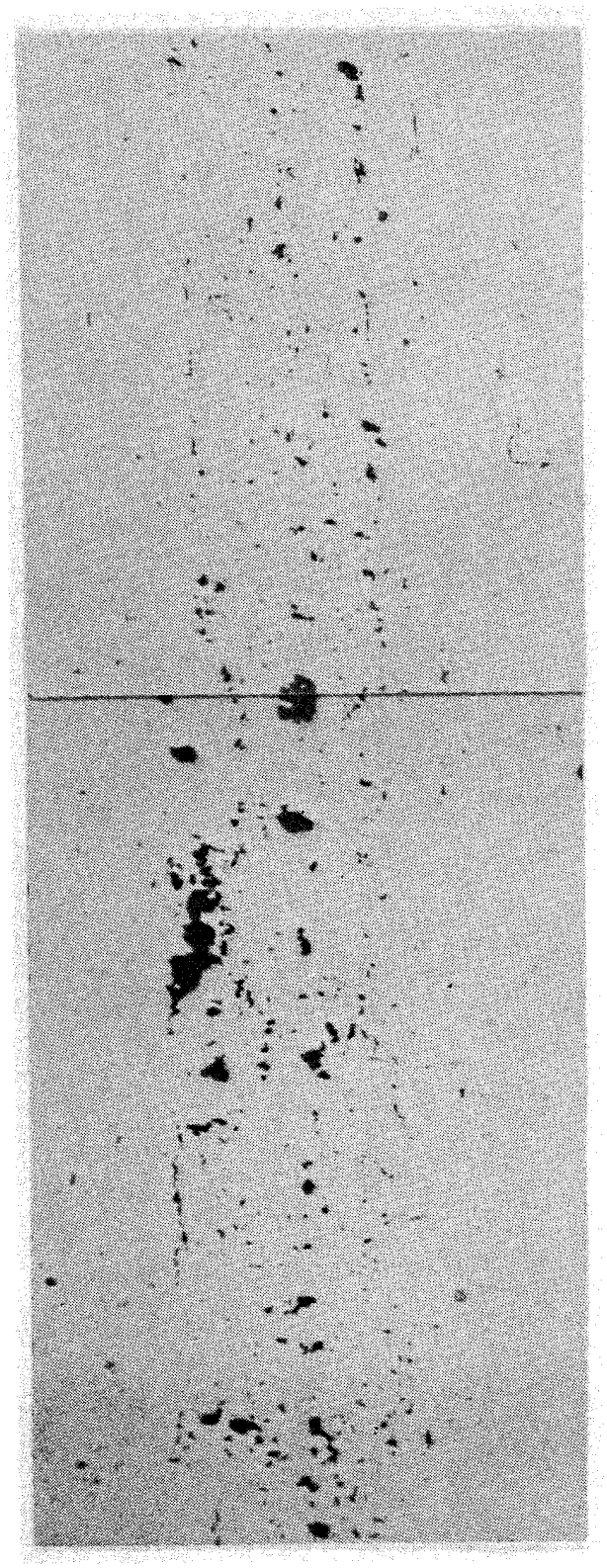

Figure 22. SEM micrograph of 8 mm thick HY100 target plate (shot #7-1690) revealing ductile void growth. Impact velocity 494 m/s.

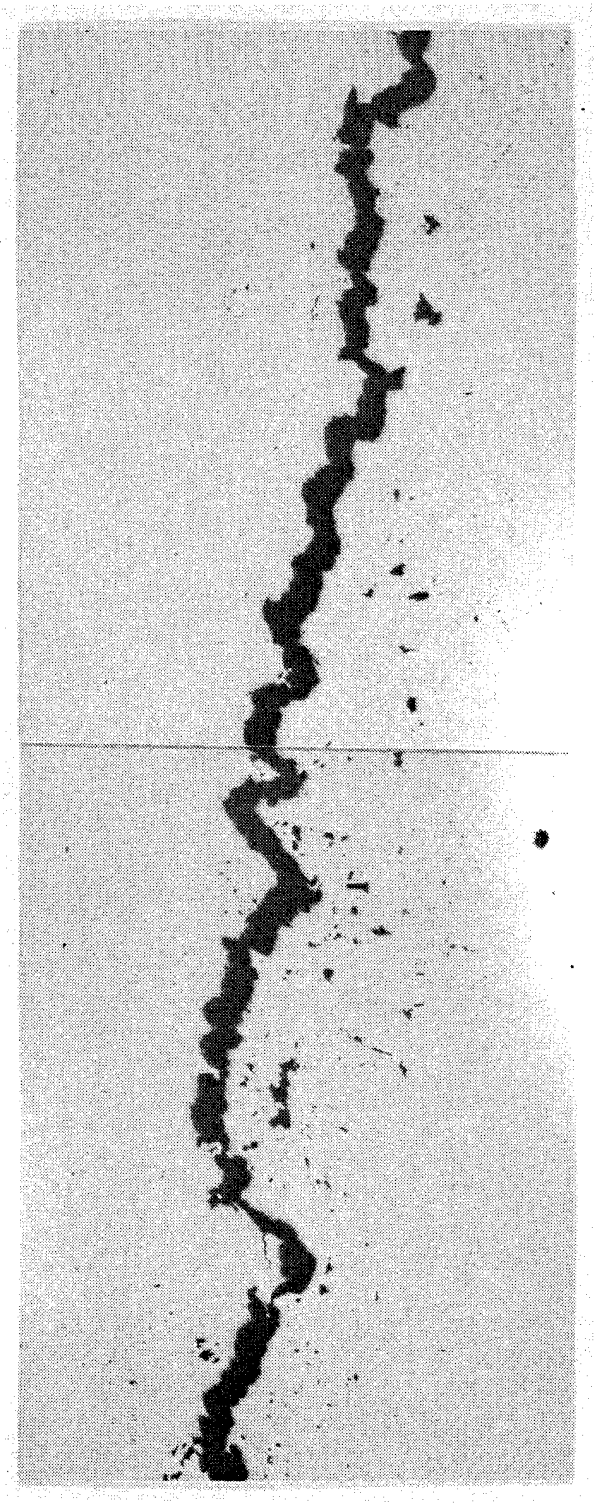

Figure 23. SEM micrograph of 8 mm thick HY130 target plate (shot #7-1688) revealing ductile void growth. Impact velocity 488 m/s.

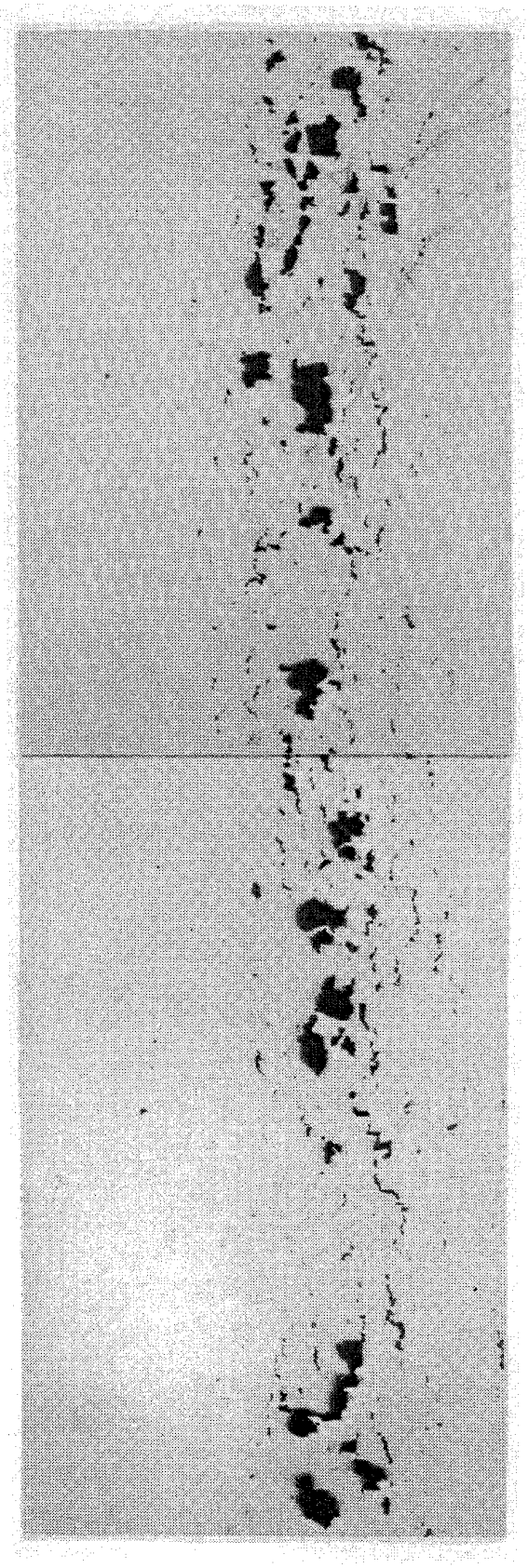

Figure 24. SEM micrograph of 8 mm thick AF1410 target plate (shot #7-1698) revealing ductile void growth. Impact velocity 536 m/s.

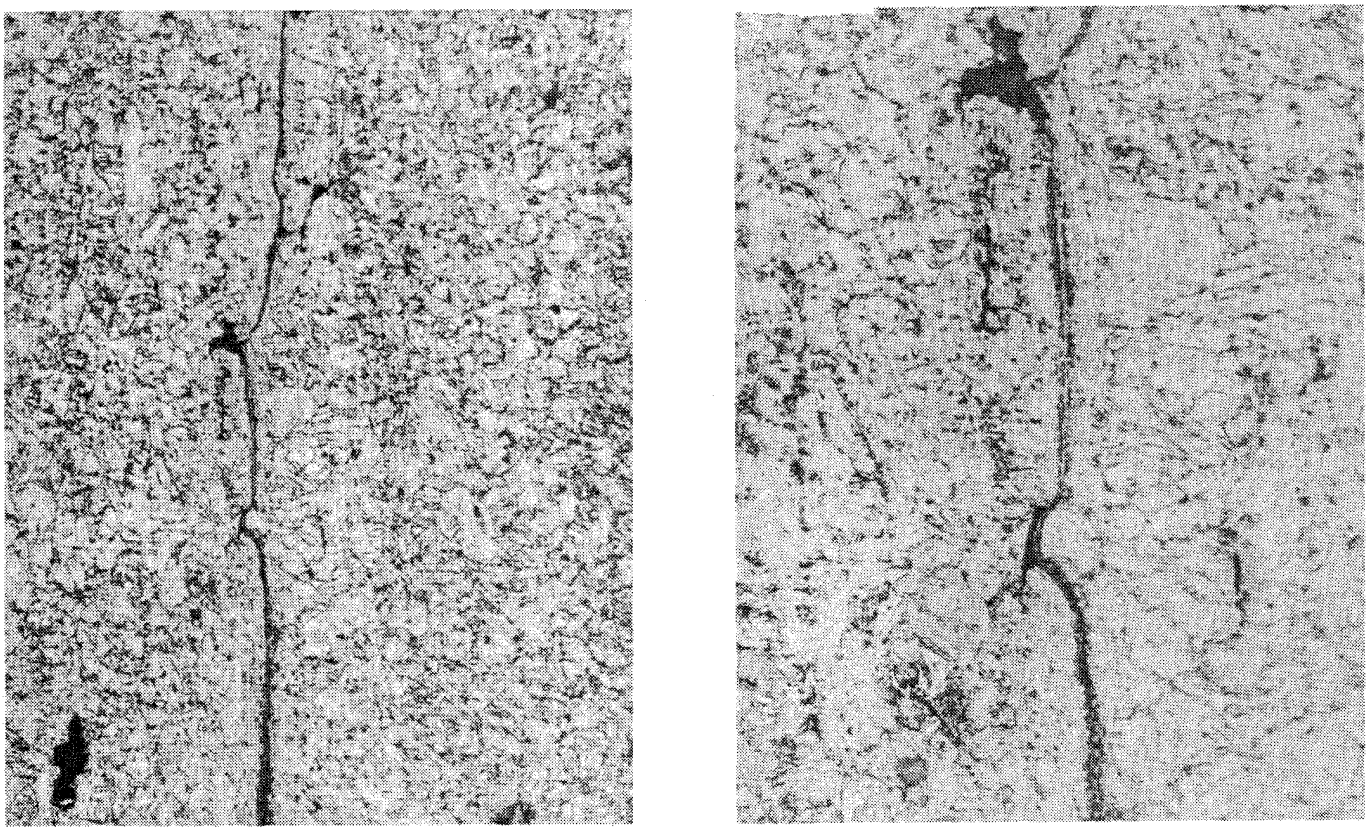

Figure 25. Optical micrographs of a localized deformation band linking two voids in an 8mm thick HY100 target plate (shot #7-1690).

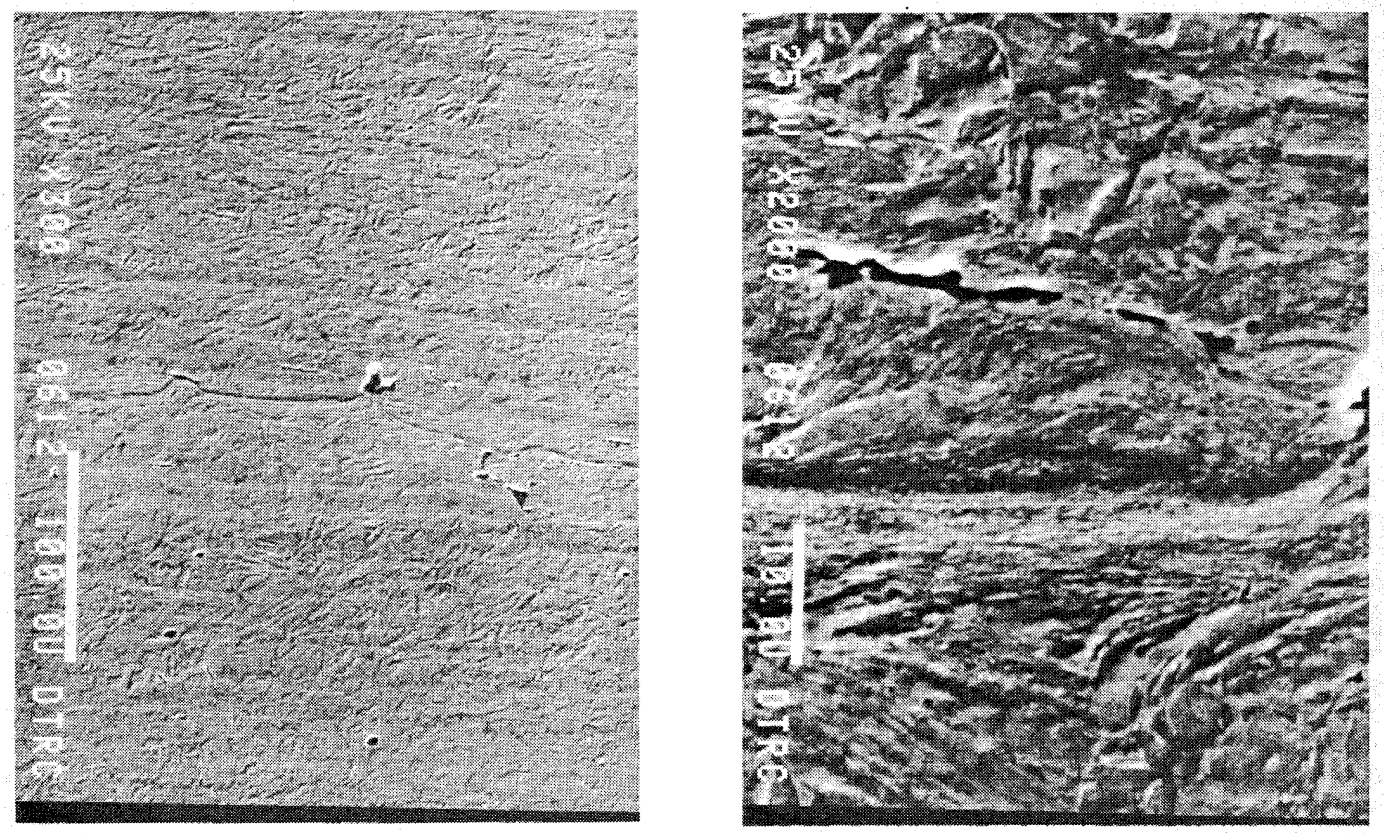

Figure 26. SEM micrographs of a localized deformation band linking two voids in an 8mm thick HY100 target plate (shot #7-1690).

Optical observations of a couple of HY130 target plates revealed little to no tendency for shear banding. Presented in Figure 27 is an isolated example of what appears to be a broad shear band in an HY130 target plate. The band etched "white" indicating that it is a transformed band. However, the width of the band being greater then 10 to 20μm is inconsistent with a transformed band. Once again, further research is needed to determine the type of the shear band and the conditions under which the band will form in this steel.

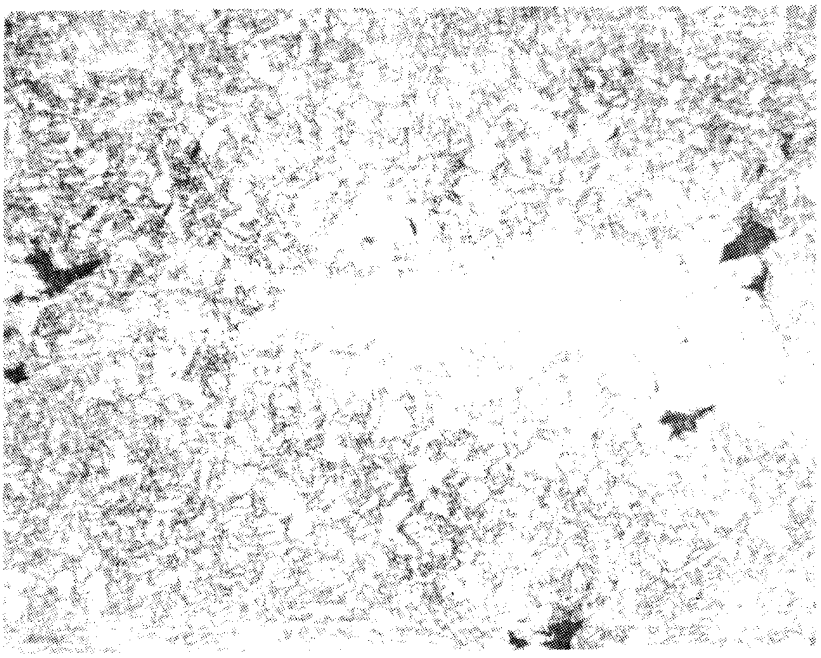

Figure 27. Optical micrographs of an isolated broad deformation band in the region of voids in an 8mm thick HY130 target plate (shot #7-1688).

The AF1410 target plate observed exhibited numerous bands of localized deformation between voids, Figure 28. These bands etched dark, consistent with deformed bands. However, SEM micrographs presented in Figure 29 reveal a narrow, possibly transformed region within the band. Further microscopic studies (most likely transmission electron microscope studies) would need to be performed to determine the type of band that occurred.

Presented in Figure 30 are SEM micrographs from a spalled fracture surface from an AF1410 target plate. There appear to be three distinct regions on this fracture surface: i) areas of larger voids that contain particles, ii) regions adjacent to the larger voids that are subjected to extensive shearing, and iii) regions with smaller voids that contain particles. The regions of larger and smaller voids are separated by the sheared region. These observations suggest that the larger voids form earlier in the failure process. Localized deformation (shearing) occurs as the larger voids grow and attempt to coalesce. The smaller voids form within the bands, void sheeting. Further studies would be needed to correlate the fracture surface features with the mechanism by which failure occurred.

**e. Further Discussions**

This summary discussion on fracture surface analysis is intended to indicate areas where further cooperation between material analysts and material modelers may prove beneficial. The relationship between material behavior and test conditions is not always easily obtained or understood. For example, the failure process of microvoid nucleation, growth and coalescence is influenced by the development of necking in the tensile samples. The onset and growth of necking are influenced by several factors. These factors, including sample geometry, test conditions, and material properties. Consequently, caution must be exercised when comparing results from various tests.

Information regarding damage accumulation from fracture surfaces is useful. However, this is just the starting point for incorporating material analysis into the modeling efforts. As discussed above, consider what may be involved in the incorporation of test condition dependence in a damage accumulation model. The damage accumulation model usually contains terms involving the nucleation and growth of microvoids, with failure occurring at a critical volume fraction of voids. The incorporation of test condition dependence may be approached as simply mathematically introducing the influence of test condition ( $\dot{\varepsilon}$ , $T$ , ) and loading history on the initial void volume fraction, the void nucleation rate, and/or the void growth rate.

These adjustments to the model should be consistent with the material and the microstructural response (e.g. plastic deformation) of the material to the test conditions. For example, the initial void volume fraction should be consistent with the volume fraction of second phase particles at which the voids nucleate. The effectiveness of various second phase particles at nucleating voids may be dependent upon temperature and rate of loading. Also, the relative contribution of void nucleation versus void growth may be related to microstructural features and test conditions. This is reflected in the results for AF1410, Figure 21d, where smaller voids (void sheets) are observed between larger voids. It appears that microvoids formed at secondary sites after a certain amount of void growth occurred at the primary sites. At this stage in the deformation/failure process, void nucleation at the secondary sites may control the process. Additional testing and analysis would need to be performed to address this issue.

The observation of spallation within each steel target plate appears to be consistent with the observations made on the tensile sample fracture surfaces. Indicating that for all test conditions employed the steels failed in a ductile manner. However, the observation shear bands within the target plates linking the voids indicates that there is a possibility that the void linking mechanism leading to fracture of each steel may depend upon test condition. Additional testing and analysis would need to be performed to further study the observed differences in the material behavior with changes in test conditions.

The material models employed should incorporate the observed test condition dependence in a manner that is consistent with the microstructural analysis. The modeling efforts may then, in turn, guide the microstructural analysis in obtaining necessary information to delineate differences in material behavior. Also, if a complete understanding of the material behavior is obtained, it may be possible to develop materials with specific properties tailored to the material or part operating conditions.

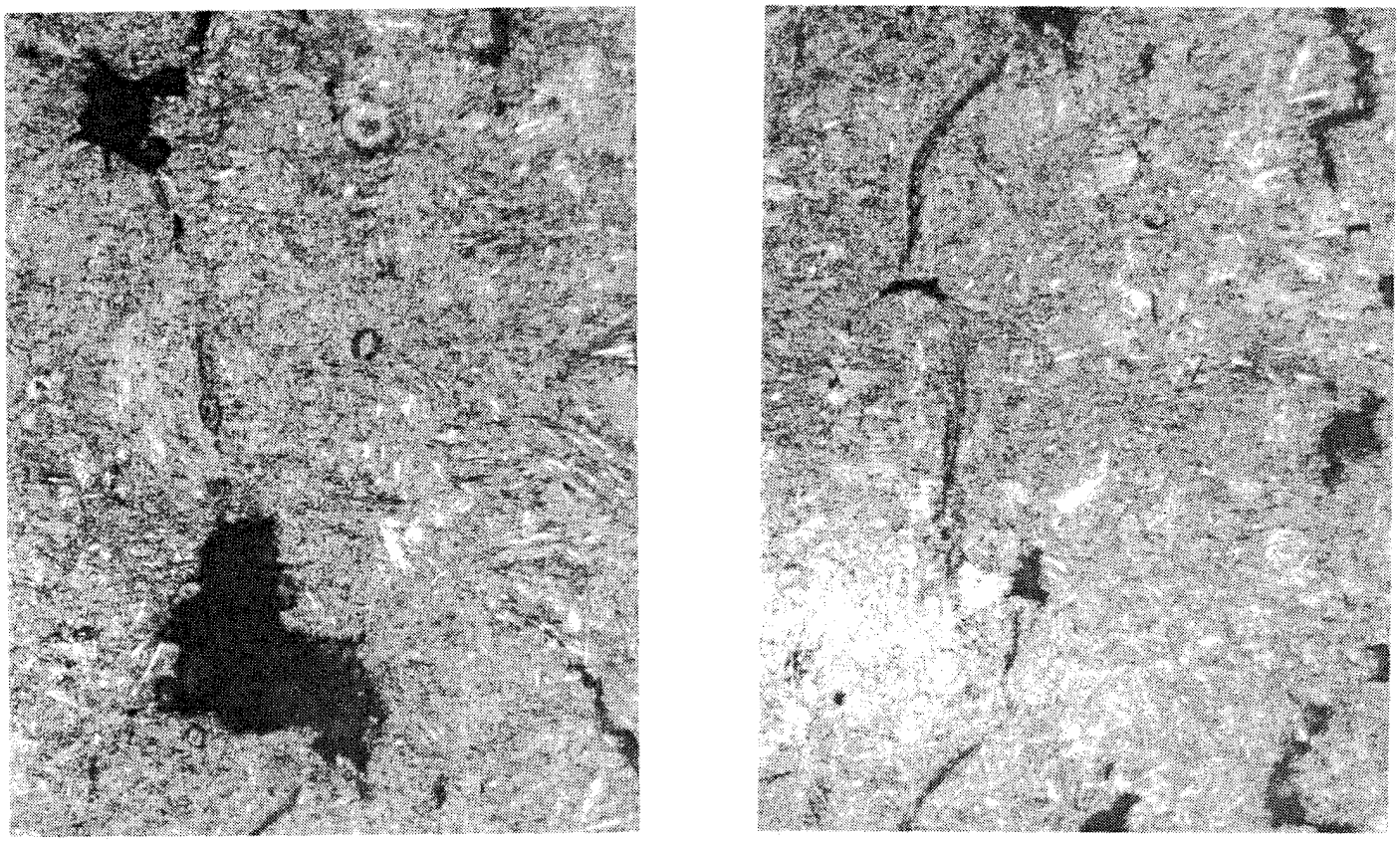

Figure 28. Optical micrographs of a localized deformation band linking two voids in an 8mm thick AF1410 target plate (shot #7-1698).

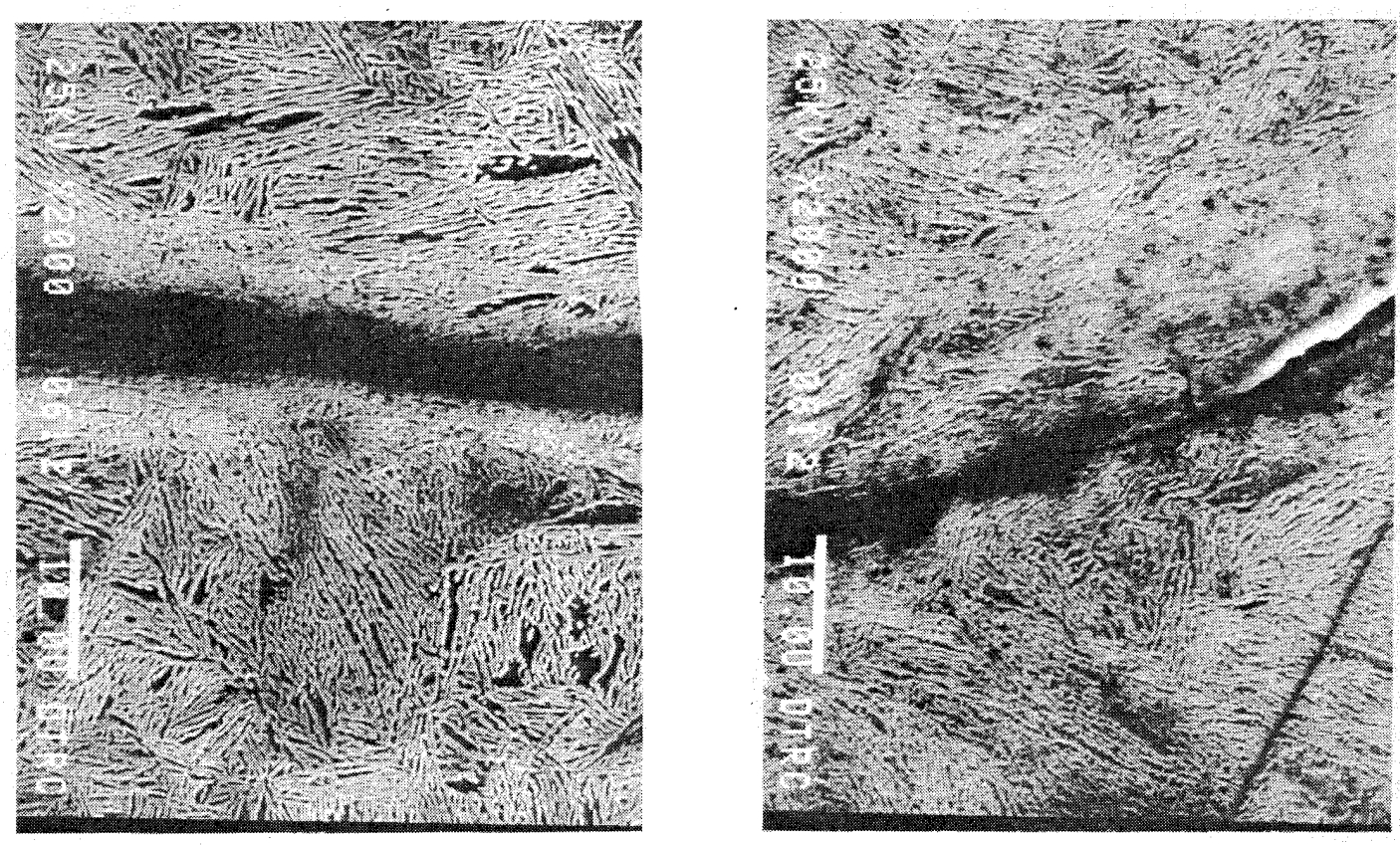

(a) (b)

Figure 29. SEM micrographs of a localized deformation band (a) between two voids and (b) at a void in an 8mm thick AF1410 target plate (shot #7-1698).

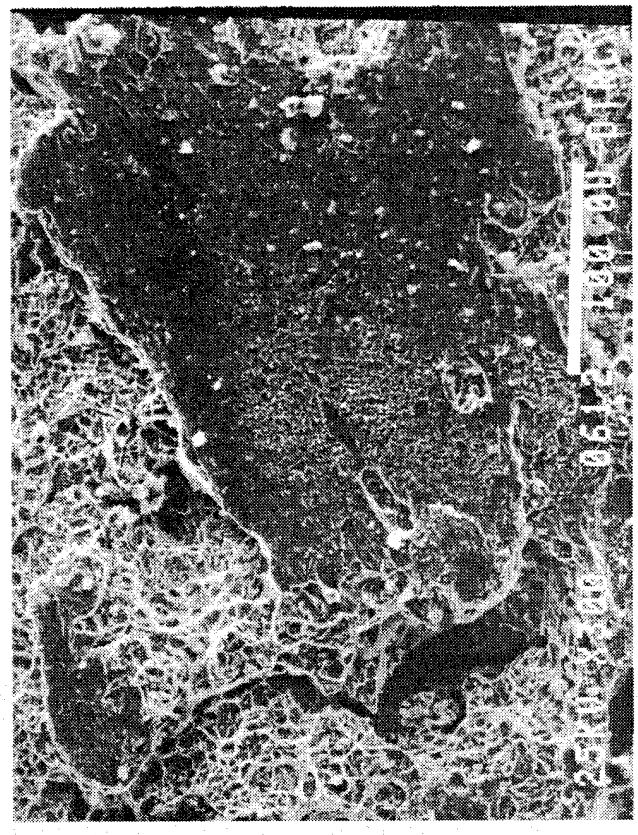

(a)

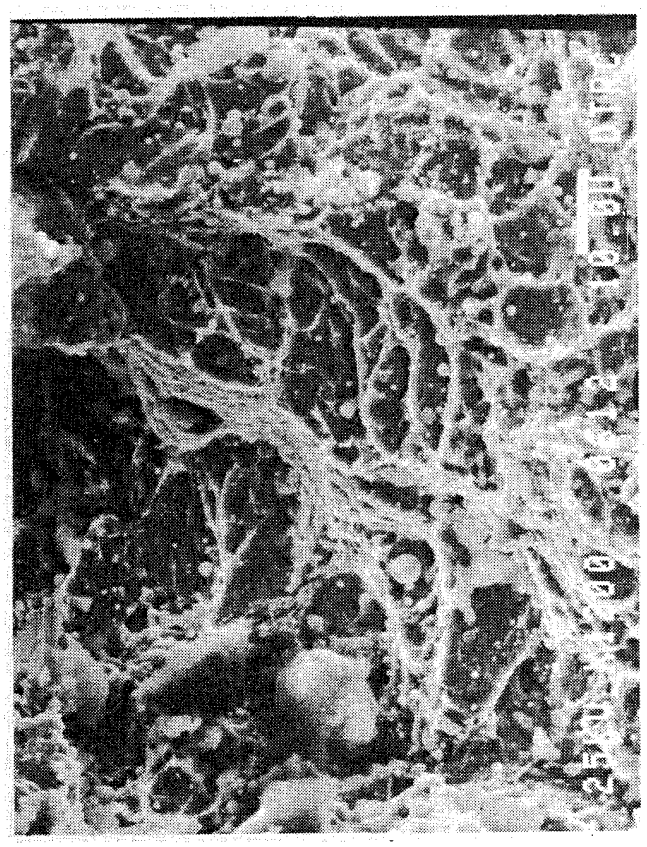

(b)

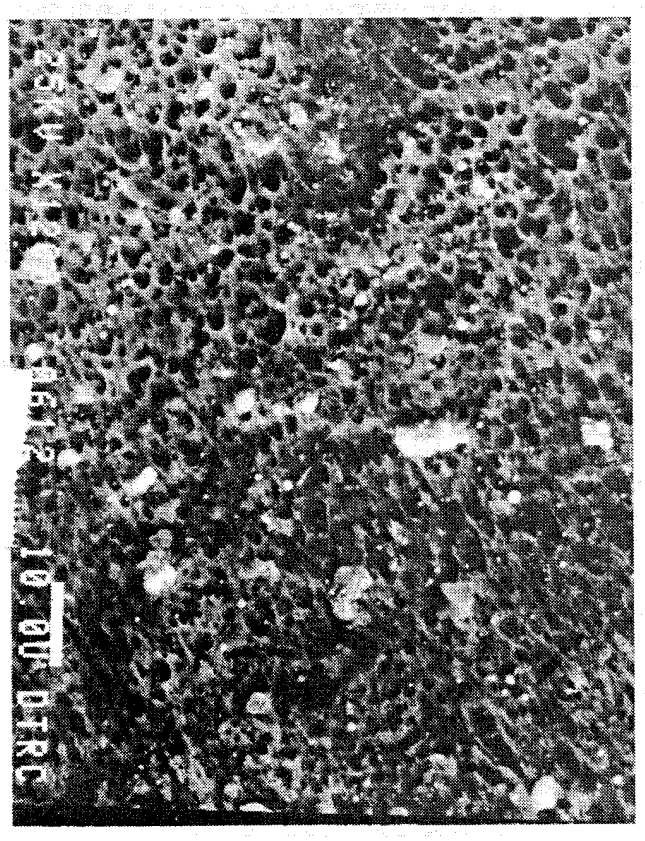

(c)

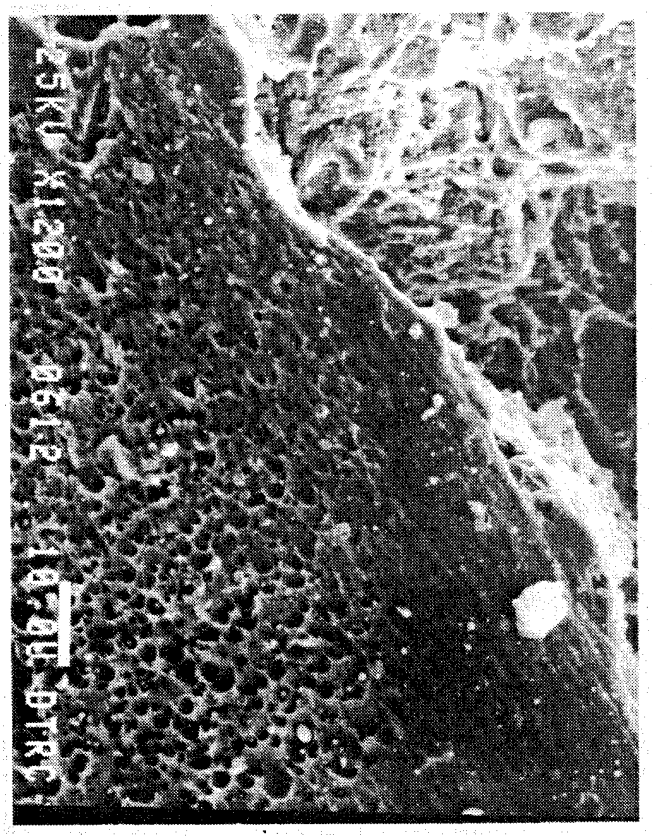

(d)

Figure 30. SEM micrographs of a completely spalled fracture surface (AF1410) (a) low magnification showing three distinct areas on surface, (b) region having larger voids with imbedded particles, (c) region having smaller voids with imbedded particles, and (d) region of 'smearing' indicating fast fracture.

## 5. Plastic Flow and Failure Modeling

The Johnson-Cook (JC) [1] and Bodner-Partom (BP) [2] models are considered in the description of strain rate and temperature dependent plastic flow in HY100, HY130, and AF1410 steels. One of the main objectives of the present work is to determine the strength model parameters using the wide range of stress-strain data from QS and SHB tests as well as the stress history data from the plate impact experiments. Strength and failure models are essential in advanced impact design calculations using hydrocodes. The JC and BP strength models are briefly described in subsections 5.1 - 5.3.

Rajendran, Dietenberger, and Grove [3] proposed a ductile failure model based on microvoid nucleation and growth. Three of the main features in this dynamic ductile failure model are the following: (1) a constitutive description of the initial intact (void-free) material which includes strain rate and temperature effects; (2) a mathematical description of the void nucleation and growth process; and (3) pressure dependent plastic flow equations for the porous (void-containing) aggregate. The RDG ductile failure model is briefly described in subsections 5.4 - 5.5. More detailed descriptions of this model and its capabilities have been published in References [18-20].

### 5.1 Johnson-Cook Model

The Johnson-Cook strength model [1] provides realistic solutions to hydrocode simulations of a broad class of dynamic events such as impact, penetration, and explosive acceleration of metals. The JC model is described by the following two equations:

$$Y = \left[A + B\,\varepsilon^{n}\right]\left[1 + C\,ln\,\dot{\varepsilon}^{*}\right]\left[1 - T^{*m}\right] \tag{5}$$

$$T^{*} = \frac{T - T_{room}}{T_{mlt} - T_{room}} \tag{6}$$

Y is the flow strength, $\varepsilon$ is effective plastic strain, $\dot{\varepsilon}^{*}$ is non-dimensional (effective plastic) strain rate (normalized by 1/sec), $T^{*}$ is homologous temperature, $T_{mlt}$ is the temperature at melting, and T is the applied temperature. The five material constants are defined as follows: A is the static yield strength, B is the strain hardening coefficient, n is the strain hardening exponent, C is the strain rate coefficient, and M is the thermal softening exponent. The model constants A, B, and n are determined from quasi-static stress-strain data either from tensile or compressive tests. The strain rate dependent constant C is determined from the slope of the stress vs. strain rate plot. The temperature constant M is estimated from the stress vs. temperature plot.

### 5.2 Bodner-Partom Model

The Bodner-Partom model [2] is briefly described in this section. The plastic strain rate is assumed to be a function of stress, $\sigma_{ij}$, a state variable, Z, and to follow the Prandtl-Reuss flow rule,

$$\dot{\varepsilon}^{p}_{ij} = \dot{e}^{p}_{ij} = \lambda S_{ij} \tag{7}$$

where $\dot{e}^{p}_{ij}$ are the deviatoric plastic strain rates. Squaring Equation (7) gives

$$D_2^p = \lambda^2 J_2 \tag{8}$$

where $D_2^p$ and $J_2$ are the second invariants of the plastic strain rate and deviatoric stresses, respectively.

$$D_2^p = D_o^2 \exp\left[-\left(\frac{Z^2}{3J_2}\right)^n \left(\frac{n+1}{n}\right)\right] \tag{9}$$

where $D_o$ is the limiting value of the plastic strain rate in shear, and n is a parameter that is mainly related to strain rate sensitivity. Z, a measure of the overall resistance of the material to plastic flow, depends on the loading history. The above equation can be rewritten in the following manner:

$$Y = Z\left[-\frac{2n}{n+1}\ln \dot{\epsilon}^*\right]^{-\frac{1}{2n}} \qquad where \quad \dot{\epsilon}^* = \frac{\sqrt{D_2^p}}{D_0} \tag{10}$$

Z is assumed to be a function of the plastic work, $W_p$:

$$Z = Z_1 - (Z_1 - Z_o)\, e^{-mW_p} \tag{11}$$

$Z_o$ is the initial value of Z, $Z_1$ is the maximum value that Z can attain, and m is a parameter that describes the strain hardening behavior of the material. The effect of temperature on the flow stress is included through the parameter n. Based on quasi-static experimental evidence, the parameter n is assumed to vary as an inverse function of absolute temperature (T):

$$n = A + \frac{B}{T} \tag{12}$$

where A and B are model parameters and T is expressed in either degrees Rankine or degrees Kelvin. Thus the BP model contains five principal material parameters ($D_o$, $Z_o$, $Z_1$, m, and n) that have to be evaluated from high strain-rate experiments of room temperature. In high strain rate applications, the limiting strain rate $D_o$ has been assumed to be $10^8$/sec for metals. This eliminates the task of determining one more model constant. Therefore, the BP model generally requires only 4 material model constants for room temperature applications. For high temperature applications, since n is a function of temperature,

one additional constant is required. Several articles on the results from using the BP model in hydrocodes can be found in References 21 - 23.

### 5.3 Strength Model Constants

The strength model (BP or JC) constants are determined using the stress - strain data from QS and SHB tests. Johnson and Holmquist [24] provided a methodology to obtain JC model constants using the data from compressive and torsional tests. Since necking type failure does not occur in these tests, stress-strain data cover large strains (> 50%). Rajendran, Bless, and Dawicke [21] mostly employed stress-strain data obtained under tensile loading and described a calibration scheme for evaluating BP model constants. The HEL (Hugoniot elastic limit) data from plate impact experiments are also included in this scheme. Tables 6-8 provide the JC and BP strength model constants for HY100, HY130, and AF1410 steels.

**Table 6. Johnson-Cook model constants**

| Material | A (kbar) | B (kbar) | n | C | m |
|---|---|---|---|---|---|
| HY100 steel | 7.6 | 4.0 | 0.26 | 0.011 | 1.13 |
| HY130 steel | 9.2 | 3.3 | 0.39 | 0.008 | 1.15 |
| AF1410 steel | 15.0 | 6.5 | 0.18 | 0.005 | 0.73 |

**Table 7. Bodner-Partom model constants**

| Material | n | $Z_o$ (kbar) | $Z_1$ (kbar) | m ($kbar^{-1}$) |
|---|---|---|---|---|
| HY100 Steel | 2.95 | 14.5 | 17.0 | 3.0 |
| HY130 Steel | 3.80 | 14.5 | 16.5 | 2.5 |
| AF1410 Steel | 5.50 | 23.0 | 26.5 | 1.5 |

**Table 8. Thermal constants for the Bodner-Partom model**

| Material | A | B (°K) | n at 400°C | n at RT |
|---|---|---|---|---|
| HY100 steel | 1.430 | 454 | 2.1 | 2.95 |
| HY130 steel | 1.470 | 694 | 2.5 | 3.80 |
| AF1410 steel | -0.230 | 1707 | 2.3 | 5.50 |

In the BP model, higher values of the rate sensitivity parameter n imply lower strain rate sensitivity in the material. From Table 7, one can see that HY130 and AF1410 steels are modeled as relatively lower rate dependent materials compared to HY100. Using the values for A and B in Table 8, values for the strain rate sensitivity parameter n at 400°C and room temperature are also given in the table. For example, the value of n is 2.1 for HY100 steel at 400°C compared to the room temperature value of 2.95. According to the experimental data, the strain rate dependency in HY100 steel did not significantly change with temperature (see Figure 8).

However, this is not the case with the other two steels (HY130 and AF1410). These two steels did not exhibit strain rate dependency at room temperature; however, they exhibited rate dependent behavior at 400°C, as reflected in the values of n. Thus, the tabulated JC and BP model constants describe the material flow stress (strength) variation with respect to both strain rate and temperature.

Since the JC and BP models constants were determined from the same set of experimental data, the two sets of constants should produce comparable stress-strain curves for various strain rates and temperatures. This was verified for temperatures between room and 400°C and strain rates between 0.001/s and 2000/sec. However, when extrapolated to extremely high strain rates, these models produce different levels of flow stress. This particular point is demonstrated in Figure 31.

As one can see from this figure, the flow stresses (at a strain of 0.05), as predicted by the two models matched extremely well below a strain rate of $10^4$/sec. However, the BP model predicted flow stress above a strain rate of $10^6$/sec was much higher than the stress levels predicted by the JC model. The JC model assumes a linear variation of flow stress with respect to a logarithmic strain rate. On the contrary, the BP model relationship (see Equation 10) was motivated by equations proposed to relate dislocation velocity to stress. This limiting-strain-rate based relationship leads to rapid increase of the flow stress when the strain rates reach the limiting strain rate, as depicted in Figure 31 for the three steels.

The difference in the variation of flow stress with respect to strain rate between various models is of great academic interest in the theoretical formulation of viscoplastic behaviors of materials. However, Cook et al., [22] reported that the use of either strength model (BP or JC) yielded very similar results in many typical impact application problems.

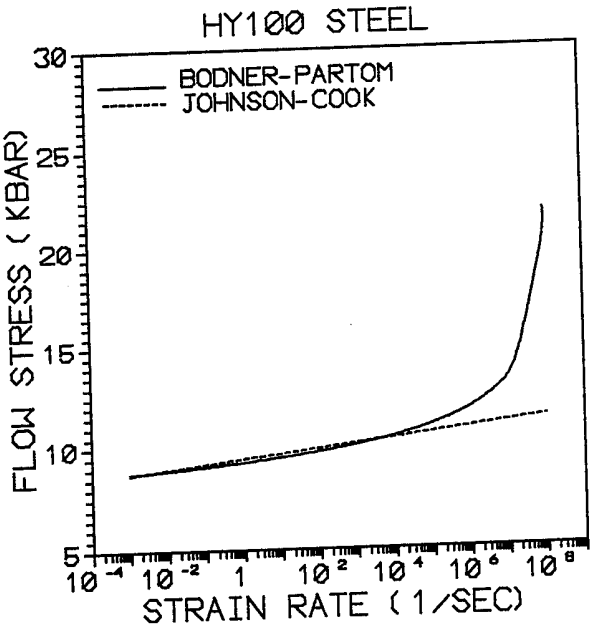


(a)

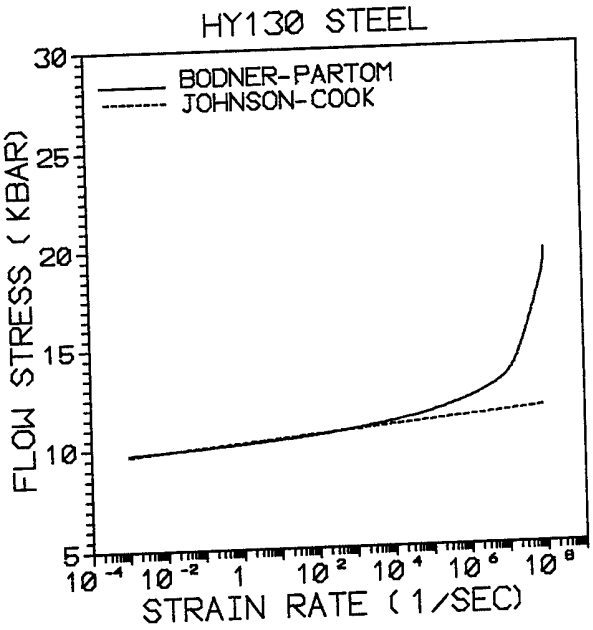


(b)

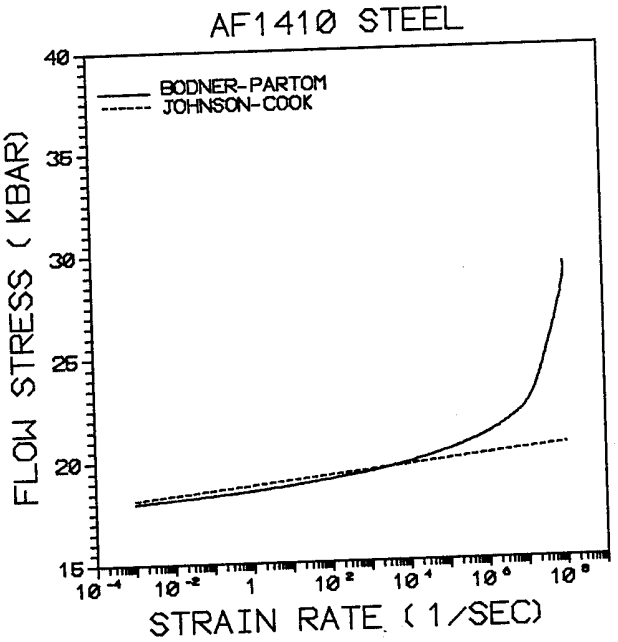


(c)

Figure 31. A comparison between JC and BP model generated flow stress vs. strain rate curves. a) HY100, b) HY130, and c) AF1410.

### 5.4 RDG Ductile Failure Model

Metallurgical observations on the fracture surfaces of tensile specimens as well as the spalled target plates confirmed the nucleation, growth, and coalescence of microvoids in the three steels. The RDG ductile failure model [3] was formulated based on microvoid nucleation and growth. This subsection provides a brief description of this model. A pressure dependent yield-criterion-based approach is considered in the constitutive model formulation. For randomly distributed voids contained in the aggregate, the yield behavior is influenced not only by the second invariant of the deviatoric stress ($J_2$) but also by the pressure or mean stress ($I_1$). The following new yield function was considered:

$$\Phi = (2+\rho^2)\, J_2 + \frac{1-\rho^2}{3} I_1^2 - \delta(\rho)\, Y_m^2 = 0 \qquad (13)$$

where,

$$\delta(\rho) = \frac{g(\rho) - g(\rho_{cr})}{g(1) - g(\rho_{cr})} \qquad (14)$$

and

$$g(\rho) = \left(\frac{1}{\kappa + f}\right), \qquad where \quad f = 1-\rho \qquad (15)$$

where $Y_m$ is the effective yield stress in the matrix material, $\kappa$ is a model constant, $\rho$ is the relative density, and f is the void volume fraction. Numerical simulations of a plate impact test configuration were performed to evaluate the effects of the $\delta$ function on the spall signal. In these simulations, the initial slope of $\delta(\rho)$ at $\rho$=1 greatly influenced the slope of the spall signal. Consequently, the parameter $\beta$ (=$\delta'(1)$) was introduced. With $\beta$ and $\rho_{cr}$ as model constants, the corresponding value of $\kappa$ can be solved by a simple iterative scheme. An idealistic value of zero can be assumed for $\rho_{cr}$, the critical relative density for void coalescence (complete failure).

The viscoplastic strain rates $\dot{\varepsilon}_{ij}^{p}$ in the aggregate can be calculated using the flow rule derived from the yield function given by Equation (13). An expression for $\dot{\sigma}_{ij}$ can be obtained from Hooke's law (elastic stress-strain relationship) by defining the elastic strain rate as the difference between the total and plastic strain rates,

$$\dot{\sigma}_{ij} = E_{ik} \left( \dot{\varepsilon}_{kj} - \dot{\varepsilon}^{P}_{kj} \right) \tag{16}$$

The evolution laws for the void content f (void volume fraction, f = 1-ρ) are given by the nucleation and growth equations. The total rate of change of void volume fraction is expressed as the sum of its nucleation and growth components:

$$\dot{f} = \dot{f}_n + \dot{f}_g \tag{17}$$

The void volume fraction nucleation rate is:

$$\dot{f}_n = F \left( \dot{Y}_m + \dot{P} \right) \tag{18}$$

with

$$F = \frac{f_0}{s\sqrt{2\pi}} e^{-\frac{1}{2}\left(\frac{Y_m + P - \sigma_N}{s}\right)^2} \tag{19}$$

$Y_m$ is the effective stress in the matrix, P is the pressure in the aggregate, and $\sigma_N$ is the mean equivalent stress around which the nucleation stress is distributed in a Gaussian manner. The term s is the standard deviation of the distribution. This parameter controls the range of stress over which the voids can be nucleated. The term $f_0$ defines the maximum allowable void volume fraction due to nucleation. The growth law can be directly related to the dilatation due to growth of voids in the aggregate. By definition, the void growth rate is given by,

$$\dot{f}_g = \frac{3 \rho^2 \dot{D}^P_m \left( 1 - \rho^2 \right)}{\delta(\rho)} \left( \frac{P}{Y_m} \right) \tag{20}$$

A strain rate dependent relationship between $Y_m$ and the equivalent plastic strain rate in the matrix material is provided by either the JC model (Equation 5) or the BP model (Equation 10).

## 5.5 RDG Model Constants

The RDG model parameters were calibrated using the manganin-gauge-measured stress histories from the plate impact experiments. There are four failure model constants: $f_0$, $\sigma_N$, s, and $\beta$. The maximum possible void volume fraction due to nucleation is arbitrarily restricted to one percent (0.01). This value was successfully used earlier by Rajendran et al. [18] for several metals. Based on a parametric study, a value of one fourth of $\sigma_N$ was assigned to the standard deviation "s" that appears in the nucleation model. Therefore, the RDG model requires calibration of only two constants: $\sigma_N$ and $\beta$. The best values for these two constants were obtained for each steel by matching the simulated stress history with the manganin gauge data. The corresponding constants are tabulated in Table 9.

**Table 9. RDG failure model constants**

| Materials | $\sigma_n$ (GPa) | $\beta$ |
|---|---|---|
| HY100 Steel | 3.6 | 30 |
| HY130 Steel | 4.8 | 50 |
| AF1410 Steel | 5.6 | 100 |

Rajendran et al. [18] reported a set of constants for HY100 steel, obtained by matching the measured stress gauge profile in a plate impact experiment (#1299) in which a 3 mm copper plate impacted a 6 mm HY100 steel plate. In this original set of constants, the void volume fraction due to nucleation ($f_0$) was assumed to be 0.035. Using the revised BP model constants for HY100 (see table 7), we repeated the simulation of this experiment with $f_0 = 0.01$, without changing the other RDG model constants. The model generated stress history (using $f_0 = 0.01$) matched the measured stress gauge profile very well as shown in Figure 32.

Employing this revised set of constants, test #7-1690 was modeled. The comparison between the model generated stress-time history and the data is shown in Figure 33. The overall matching was reasonable. We also simulated test # 7-1693 in which a 2 mm HY100 steel flyer impacted an 8 mm HY100 steel target. The comparison between the RDG model predicted stress vs. time history and the manganin gauge data is shown in Figure 34. The model did not exactly follow the data; this could be attributed to scatter in the experimental data.

Unfortunately, the original manganin gauge traces for all the tests reported in Table 4 were unusually noisy. The data were altered (or smoothed) prior to predicting the plate impact test results using

the RDG model. Comparisons between the manganin gauge data from two identical tests (#7-1691 and #7-1692) and the RDG model prediction are presented in Figure 35. The geometry and impact velocity in the two tests were almost identical (see Table 4). However, there was significant scatter in the experimentally measured shock stress (peak stress) and spall signal. Therefore, it is not possible to judge the model prediction for accuracy. As can be seen from Figure 35, the model prediction of the stress - time history was somewhat an average between these two tests.

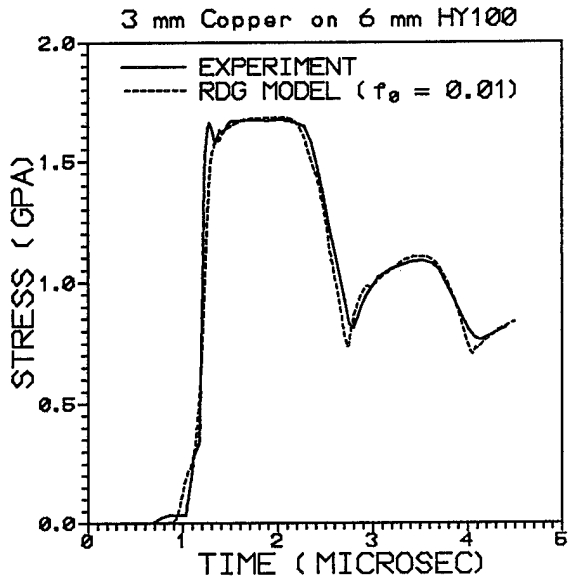


Figure 32. A comparison between RDG model prediction and manganin gauge data for test #1299.

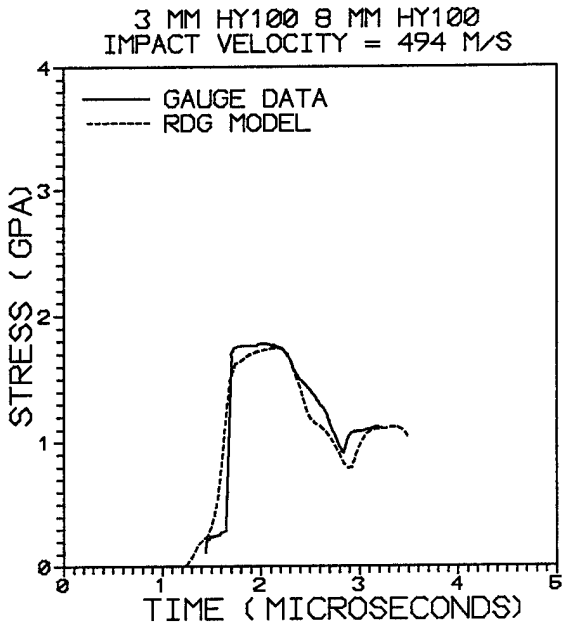


Figure 33. A comparison between RDG model prediction and manganin gauge data for test #1690.

Figure 36 compares the stress history from test #7-1686 with the model-generated stress history for HY130 steel. The experimental trace beyond 4.3 microseconds (μs) was noisy and therefore, the portion of the trace beyond 4.3 μs is not shown in the figure. The RDG model reproduced the measured spall signal reasonably well. Employing the same constants, test #7-1688 was simulated and the predicted results are compared with the data in Figure 37. In this test, the gauge failed at about 2.4 μs. The RDG model predicted most of the salient features of the gauge trace.

Four plate impact tests on AF1410 steel were also simulated using the RDG model. The flyer thicknesses in these tests varied from 2 mm to 4 mm. The only difference between tests #1696 and #1697 is the flyer thickness. The impact velocity and the target thickness were the same in these two tests. In other words, the target was subjected to different loading pulse durations. A comparison of spall signals between the two shots shows the effect of pulse duration on the amplitude of the spall signal.

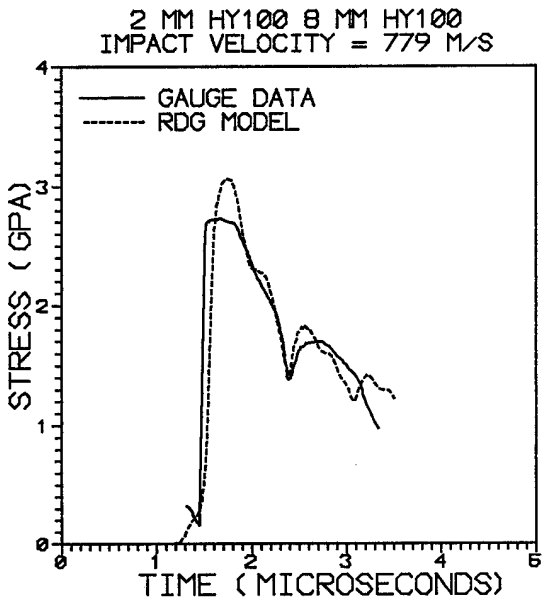


Figure 34. A comparison between RDG model prediction and manganin gauge data for test #1693.

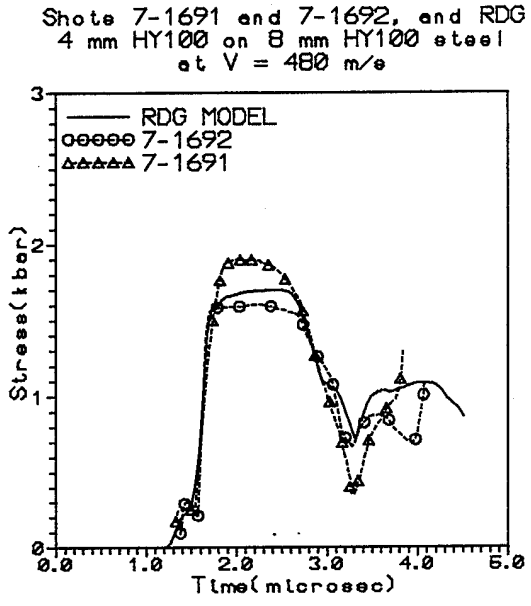


Figure 35. Comparisons between RDG model prediction and gauge data for tests 1691 and 1692.

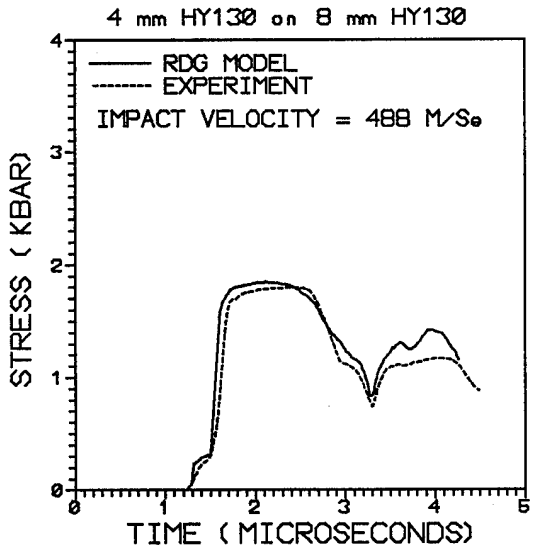


Figure 36. A comparison between RDG model prediction and manganin gauge data for test #1686.

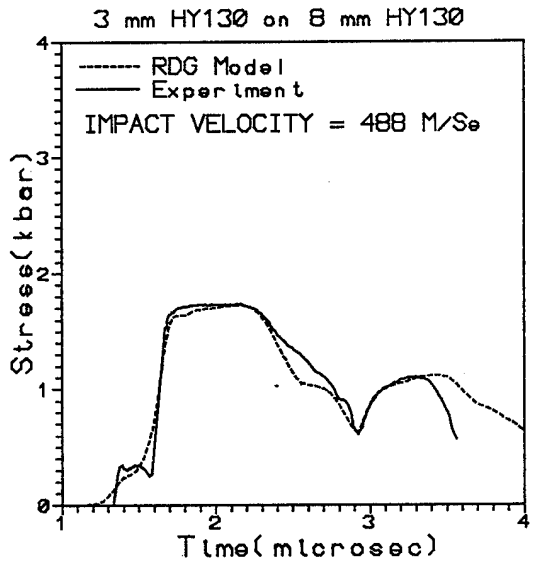


Figure 37. A comparison between RDG model prediction and manganin gauge data for test #1688.

The results are summarized in Figures 38 - 41. The model reproduced all the spall signals reasonably well. The arrival time, shapes, and amplitudes of the spall signals matched well with the measured manganin gauge data. As we mentioned earlier, the gauge signals in these experiments were unusually noisy; this led to smoothing of the experimental data, which introduced significant scatter. Taking this point into consideration, we can conclude that the RDG model predicted the spall evolution in the three steels extremely well.

At present the RDG model is the only advanced void growth model for which constants for various metals are available. Therefore, the availability of physically based RDG model constants will enhance our present capability in modeling the ductile failure of metals under impact loading and extreme strain rate loading conditions.

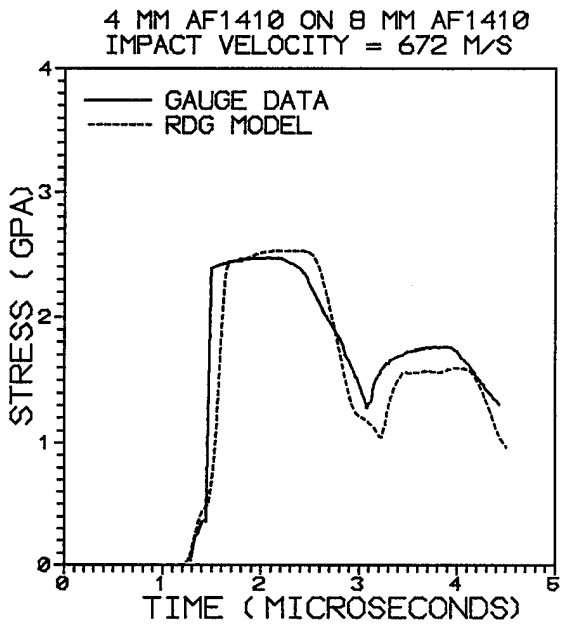


Figure 38. A comparison between RDG model prediction and manganin gauge data for test #1695.

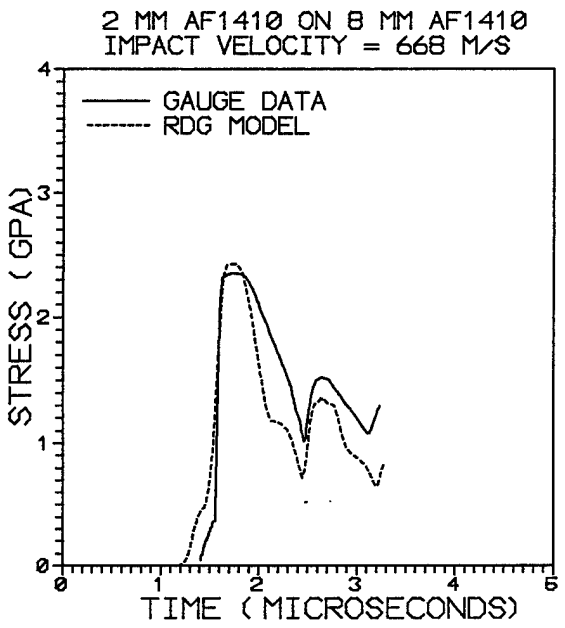


Figure 40. A comparison between RDG model prediction and manganin gauge data for test #1697.

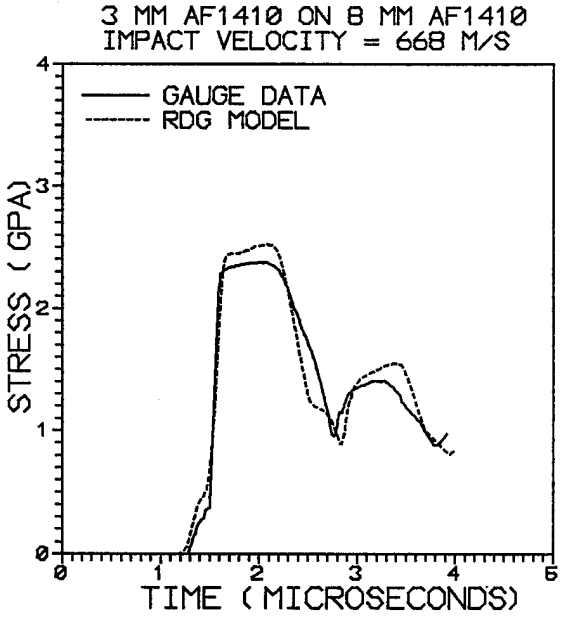


Figure 39. A comparison between RDG model prediction and manganin gauge data for test #1696.

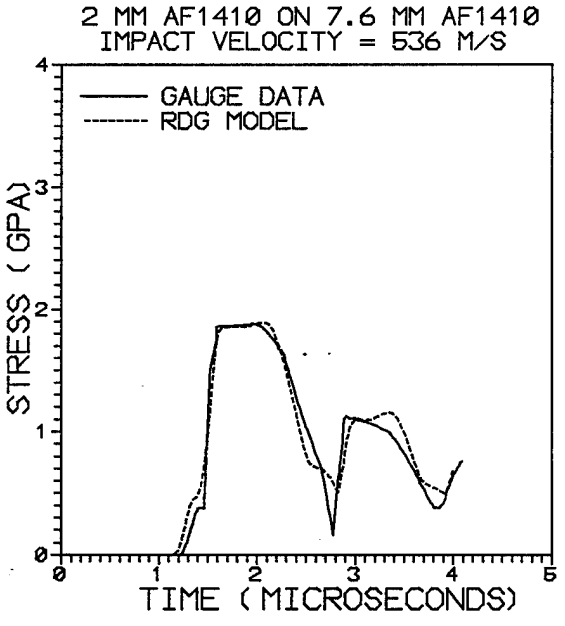


Figure 41. A comparison between RDG model prediction and manganin gauge data for test #1698.

# 6. Summary and Recommendations

## 6.1 Summary

The high strain rate and shock impact behaviors of HY100, HY130, and AF1410 steels were evaluated through a combination of experimental, metallurgical, and numerical methods. Uniaxial-stress-based split Hopkinson bar tensile tests and one-dimensional-strain-based plate impact experiments were performed. For comparison, quasi-static tensile tests were also performed. The effects of strain rate and temperature on the flow and failure behaviors were evaluated. The influence of strain rate and temperature on the strain hardening and strain rate hardening (sensitivity) were determined from the QS and SHB tests. The effects of strain rate on the thermal softening behaviors of the three steels were also investigated. Differences in the flow and failure behaviors among HY100, HY130, and AF1410 were observed through comparisons of the experimental stress-strain curves.

### a. Strain Hardening

The HY100 and HY130 steels exhibited moderate strain hardening at room temperature. Since the onset of necking occurred immediately upon initial yielding, it was not possible to evaluate the strain hardening behavior of AF1410 steel; however, lower values for the strain hardening constants were assumed (see Tables 6 and 7; n=0.18 in JC and m=1.5 in BP). For similar reasons, the influence of temperature on the strain hardening behaviors in the three steels could not be evaluated.

### b. Strain Rate Sensitivity

At room temperature, the strain rate sensitivity in AF1410 and HY130 steels was insignificant. The stress-strain curves at 0.001/sec and 1500/sec were almost identical. However, at an elevated temperature (400°C) these two steels began to exhibit moderate strain rate dependent behaviors. In general, for all three steels, the strain rate sensitivity increased at elevated temperatures, with a maximum increase in the AF1410 steel.

### c. Ductility

The ductility of HY100, HY130, and AF1410 steels drastically decreased at elevated temperature under QS loading conditions by 46%, 41%, and 55%, respectively. One explanation is that the adiabatic heating in the necked region could have accelerated the localization of deformations. However, under high strain rate (SHB) loading conditions, while the AF1410 steel retained its ductility and the HY130 retained a significant amount of ductility at elevated temperatures, the ductility of HY100 was reduced drastically by 37%. The inertial effects usually slow down the localized necking process, thereby allowing additional deformation in the uniform sections of the sample. This effect is often more pronounced in rate sensitive materials. While the AF1410 steel was rate insensitive at room temperature, it exhibited enhanced rate sensitivity at an elevated temperature; therefore, the inertial effects could have been stronger in AF1410 compared to the other steels. Unfortunately, the microstructural studies on the fractured specimen did not reveal any clues to explain the reduction in ductility at elevated temperatures.

**d. Modeling**

The quasi-static and high strain rate behaviors of the three steels were modeled using two strength models: Johnson-Cook and Bodner-Partom. The strain hardening, strain rate hardening, and thermal softening behaviors were modeled and the corresponding model constants were successfully determined. The HY100, HY130, and AF1410 steels exhibited ductile failure due to void nucleation, growth, and coalescence under QS, SHB, and shock loading conditions. This process was modeled using the RDG model [3]. The measured spall signals from plate impact experiments were reproduced using this model. The RDG model constants were successfully determined for these steels. There are four constants in the RDG failure model: 1) the maximum allowable void volume fraction for nucleation ($f_0$), 2) the mean threshold stress for nucleation ($\sigma_N$), 3) the standard deviation of the normal distribution for nucleation (s), and 4) the constant $\beta$ that is associated with the pressure dependent yield function for a voided material. In the modeling of HY100, HY130, and AF1410 steels, $f_0$ was arbitrarily assigned a value of 0.01 (1% void) and s was assumed to be equal to one fourth of $\sigma_N$. The constants $\sigma_N$ and $\beta$ were adjusted to match the manganin gauge measured stress histories in the plate impact experiments. The JC or BP models were used to describe the intact material behavior. Using one set of RDG model constants for each steel, the spall signals in plate impact experiments were successfully predicted.

## 6.2 Recommendations

Additional work is needed to understand the fundamental reasons for reduction in ductility at an elevated temperature. Based on the microstructural studies, we were unable to establish the mechanisms that led to this reduction. To further verify the effects of temperature on the strain rate sensitivity and ductility, we recommend additional experiments at two more temperature levels, such as 200°C and 600°C, at least under quasi-static loading conditions.

The generality of the RDG model constants which characterize the void nucleation, growth, and coalescence processes in the three steels should be established by performing 2D axisymmetric EPIC simulations of the SHB tensile tests. Since the high speed photographs of the neck evolution in the tensile samples are available, the model simulated ductile failure of the SHB tensile samples can be directly compared with the photographs. This exercise will shed further light on the capabilities of the RDG model. Since the spall process occurs at high mean stress levels, the void nucleation mechanism is driven by stress rather than plastic strain. Intuitively, it appears that the nucleation process under a relatively low mean stress (dominantly uniaxial stress) loading condition may be controlled by plastic strain levels. In the model, we can employ a Gaussian distribution about a threshold plastic strain for nucleation.

In general, the availability of JC, BP, and RDG model constants will be very useful in armor/anti-armor design studies using hydrocodes. In addition, the extensive experimental data that are presented in this report will be useful for calibrating models other than the JC, BP, and RDG models.

## 7. References


1. Johnson, G. R. and Cook, W. H., **"Fracture Characteristics of Three Metals Subjected to Various Strains, Strain Rates, Temperatures and Pressures,"** *Eng. Fracture. Mech.*, 21, 31-48 (1985).

2. Bodner, S. R. and Partom, Y., **"Constitutive Equations for Elastic-Viscoplastic Strain Hardening Materials"**, *J. of Appl. Mech.*, 42, 385-89 (1975).

3. Rajendran, A. M., Dietenberger, M. A. and Grove, D. J., **"A Void Nucleation and Growth Based Failure Model for Spallation,"** *J. of Appl. Phys.*, 65, 1521-27, (1989).

4. Johnson, G. R. and Stryk, R. A., **"User Instructions for the EPIC-2 Code,"** AFATL-TR-86-51, Eglin Air Force Base, FL, (1986).

5. Grove, D.J., and Rajendran, A.M., **"Implementation and verification of the RDG Ductile Failure Model for Metals in the 1992 version of the EPIC Computer Code,"** unpublished work, Army Research Laboratory, Watertown, December 1993.

6. Johnson, G.R., and Stryk, R.A., **"User Instructions for the 1992 Version of the EPIC Code,"** Alliant Techsystems Inc., Brooklyn Park, MN 55428, September 1992.

7. G. Krauss, **Steels: Heat Treatment and Processing Principles**, ASM International, Materials Park, OH, 1990.

8. J.R. Strife and D.E. Passoja; **"The Effect of Heat Treatment on Microstructure and Cryogenic Fracture Properties in 5Ni and 9Ni Steel"**; Met. Trans. A, col 11A, Aug. 1980, pp. 1341-1350.

9. G.R. Speich, D.S. Dabkowski, and L.F. Porter; **"Strength and Toughness of Fe-10Ni Alloys Containing C, Cr, Mo, and Co"**; Metallurgical Transactions, vol. 4, January 1973, pp. 303-315.

10. Rajendran, A. M., and Bless, S. J., "Determination of Tensile Flow Stress Beyond Necking at Very High Strain Rate," Experimental Mechanics, Vol. 26, No. 4, December (1986).

11. Nicholas, T., **"Tensile Testing of Materials at High Rates of Strain,"** *Exp. Mech.*, 21, 177-185, (1981).

12. Rosenberg, Z, Dawicke, D., Strader, E., and Bless, S.J., "A New Technique for Heating Specimens Using Induction Coil Heaters," Exp. Mech., Vol. 29, No. 3, pp. 275-278, 1986.

13. Bridgman, P.W., "Studies in Large Plastic Flow and Fracture, Chapter 1, McGraw Hill (1952).

14. T.J. Holmquist, "Strength and Fracture Characteristics of HY-80, HY-100, and HY-130 steels subjected to various strains, strain rates, temperatures, and pressures," NSWC TR 88-252, Naval Surface Warfare Center Technical report, Silver Spring, MD, September (1987).

15. Rajendran, A. M. and Fyfe, I. M., "Inertia Effects on the Ductile Failure of Thin Rings," Journal of Applied Mechanics, Trans. ASME., Vol. 49, pp. 31-36, March 1982.

16. G. Regazzoni and Montheillet, "High Strain rate Ductility in Uniaxial Tension: A Review," J. of Physique Collogue, Vol. C5, No. 8, 1985, p. 435.

17. *Metals Handbook: Desk Edition*, H.E. Boyer and T.L. Gall, Eds., ASM International, Materials Park, OH, 1985.

18. Rajendran, A.M., Dietenberger, M.A., and Grove, D. J., "Results from the Recently Developed Dynamic Failure Model," Shock Compression of Condensed Matter- 1989, S.C. Schmidt, J.N. Johnson, and L.W. Davison (Editors), Elsevier Science Publishers, pp. 373-376, 1989.

19. A.M. Rajendran, S.J. Bless, and D.J. Grove, "Dynamic Ductile Failure Under Multi-Axial Loading," in "Anisotropy and localization of Plastic Deformation," Eds., J. Boehler and A.S. Khan, Elsevier Applied Science, p. 401, 1991.

20. Grove, D. J., Rajendran, A.M., and Dietenberger, M.A., "Numerical Simulation of a Double Flyer Impact Experiment," Shock Compression of Condensed Matter- 1989, S.C. Schmidt, J.N. Johnson, and L.W. Davison (Editors), Elsevier Science Publishers, pp. 365-368, 1989.

21. Rajendran, A. M., Bless, S. J. and Dawicke, D. S., **"Evaluation of Bodner-Partom Model Parameters at High Strain Rate,"** ASME *J. Eng. Mat. and Tech.*, 108, 75-80, (1986).

22. Cook, W. H., Rajendran, A. M., and Grove, D. J., **"An Efficient Implementation of the Bodner-Partom Model in an Explicit Finite Element Code,"** to appear in *J. of Eng. Fracture Mechanics*, (1992).

23. Rajendran, A. M. and Bless, S. J., "Use of the Bodner-Partom Viscoplastic Constitutive Model to Describe HY100 Steel'" Shock Waves in Condensed Matter, Y.M. Gupta, ed., Plenum Publishing Corp., pp. 383-388, (1986).

24. Johnson, G.R., and Holmquist, T.J., "Evaluation of Cylinder-Impact test Data for Constitutive Model Constants," J. Appl. Phys., Vol. 64, No. 8, pp. 3901-3910, October 1988.

DISTRIBUTION LIST

| No. of Copies | To |
|---|---|
| 1 | Office of the Under Secretary of Defense for Research and Engineering, The Pentagon, Washington, DC 20301 |
| | Director, U.S. Army Research Laboratory, 2800 Powder Mill Road, Adelphi, MD 20783-1197 |
| 1 | : AMSRL-OP-SD-TP, Technical Publishing Branch |
| 1 | AMSRL-OP-SD-TA, Records Management |
| 1 | AMSRL-OP-ST-TL, Technical Library |
| 1 | AMSRL-SS |
| | Director, U.S. Army Research Laboratory, 2800 Powder Mill Road, Adelphi, MD 20783-1197 |
| 1 | ATTN: Technical Library |
| | Commander, Defense Technical Information Center, Cameron Station, Building 5, 5010 Duke Street, Alexandria, VA 22304-6145 |
| 2 | ATTN: DTIC-FDAC |
| 1 | MIA/CINDAS, Purdue University, 2595 Yeager Road, West Lafayette, IN 47905 |
| | Commander, Army Research Office, P.O. Box 12211, Research Triangle Park, NC 27709-2211 |
| 1 | ATTN: Information Processing Office |
| 1 | Dr. Andrew Crowson |
| 1 | Dr. Kailasam Iyer |
| | Commander, U.S. Army Materiel Command, 5001 Eisenhower Avenue, Alexandria, VA 22333 |
| 1 | ATTN: AMCSCI |
| | Commander, U.S. Army Materiel Systems Analysis Activity, Aberdeen Proving Ground, MD 21005 |
| 1 | ATTN: AMXSY-MP, H. Cohen |
| | Commander, U.S. Army Missile Command, Redstone Arsenal, AL 35809 |
| 1 | ATTN: AMSMI-RD-CS-R/Doc |
| | Commander, U.S. Army Armament, Munitions and Chemical Command, Dover, NJ 07801 |
| 1 | ATTN: Technical Library |
| | U.S. Army Communications and Electronics Command, Fort Monmouth, NJ 07703 |
| 1 | ATTN: Technical Library |
| | Commander, U.S. Army Natick Research, Development and Engineering Center, Natick, MA 01760-5010 |
| 1 | ATTN: DFAS-IN-EM-TL, Technical Library |
| | Commander, U.S. Army Satellite Communications Agency, Fort Monmouth, NJ 07703 |
| 1 | ATTN: Technical Document Center |

| No. of Copies | To |
|---|---|
| | Commander, White Sands Missile Range, NM 88002 |
| 1 | ATTN: STEWS-WS-VT |
| | President, Airborne, Electronics and Special Warfare Board, Fort Bragg, NC 28307 |
| 1 | ATTN: Library |
| | Director, U.S. Army Research Laboratory, Aberdeen Proving Ground, MD 21005-5066 |
| 1 | ATTN: AMSRL-WT |
| 1 | AMSRL-WT-TA, George Hauver |
| 1 | AMSRL-WT-TD, Michael J. Scheidler |
| 1 | AMSRL-WT-TC, Kent Kinsey |
| 1 | AMSRL-WT-TD, Thomas W. Wright |
| 1 | AMSRL-WT-TD, Glenn Randers-Pehrson |
| 1 | AMSRL-WT-TD, Steven Segletes |
| 1 | AMSRL-TB-W |
| 1 | AMSRL-TB-AM |
| 1 | AMSRL-TB-P |
| 1 | AMSRL-AMB-TBD |
| 1 | William Gooch |
| | Commander, Dugway Proving Ground, UT 84022 |
| 1 | ATTN: Technical Library, Technical Information Division |
| | Air Force Materials Directorate, WPAFB, OH 45433 |
| 1 | ATTN: Dr. Theodore Nicholas |
| 1 | NASA - Langley Research Center, Hampton, VA 23665-5225 |
| | U.S. Army Vehicle Propulsion Directorate, NASA Lewis Research Center, 2100 Brookpark Road, Cleveland, OH 44135-3191 |
| 1 | ATTN: AMSRL-VP |
| | Director, Defense Intelligence Agency, Washington, DC 20340-6053 |
| 1 | ATTN: ODT-5A (Mr. Frank Jaeger) |
| | Air Force Armament Laboratory, Eglin Air Force Base, FL 32542-5434 |
| 1 | ATTN: Dr. J. C. Foster, Jr. |
| 1 | Dr. W. H. Cook |
| | Naval Post Graduate School, Monterey, CA 93943 |
| 1 | ATTN: Dr. Joseph Sternberg, Code EW |
| | Lawrence Livermore, National Laboratory, Livermore, CA 94550 |
| 1 | ATTN: J. E. Reaugh, L-290 |
| 1 | R. L. Landingham, MC L-369 |
| 1 | M. Finger, L-38 |
| 1 | Daniel J. Steinberg |
| 1 | Carl R. Cline |

| No. of Copies | To |
|---|---|
| | Los Alamos National Laboratory, Los Alamos, NM 87545 |
| 1 | ATTN: Dr. R. Karpp, M-8, J960 |
| 1 | Dr. J. Taylor, ADDRA, MS A11 |
| 1 | Dr. J. N. Johnson, T-14, MS B214 |
| 1 | Dr. P. J. Mauldlin, N-6, MS K557 |
| 1 | Dr. F. Adessio, T-3, MS B216 |
| 1 | Dr. Denise Hunter |
| 1 | Dr. Dave Mandell |
| 1 | Dr. B. M. Hogan |
| | Southwest Research Institute, 6220 Culebra Road, San Antonio, TX 78238 |
| 1 | ATTN: Dr. James Lankford |
| 1 | Dr. C. E. Anderson |
| 1 | Dr. James Walker |
| | Southwest Research International, 333 Ravenswood Avenue, Menlo Park, CA 94025 |
| 1 | ATTN: Dr. Richard Klopp |
| | Institute for Defense Analysis, 1801 N. Beauregard Street, Alexandria, VA 22311-1772 |
| 1 | ATTN: Dr. George Mayer |
| 1 | Dr. Marc A. Adams, JPL MS 97-B, 4800 Oak Grove Drive, Pasadena, CA 91109 |
| 1 | P.D. Buckley, NMIMT, TERA Group, Socorro, NM 87801 |
| | California Institute of Technology, Geophysics Division MS/252-21, Pasadena, CA 91125 |
| 1 | ATTN: Professor T. J. Ahrens |
| | Director, Benet Weapons Laboratory, LCWSL, USA AMCCOM, Watervliet, NY 12189 |
| 1 | ATTN: AMSMC-LCB-TL |
| 1 | AMSMC-LCB-R |
| 1 | AMSMC-LCB-RM |
| 1 | AMSMC-LCB-RP |
| | Commander, U.S. Army Foreign Science and Technology Center, 220 7th Street, N. E., Charlottesville, VA 22901-5396 |
| 3 | ATTN: AIFRTC, Applied Technologies Branch, Gerald Schlesinger |
| | Commander, U.S. Army Aeromedical Research Unit, P.O. Box 577, Fort Rucker, AL 36360 |
| 1 | ATTN: Technical Library |
| | U.S. Army Aviation Training Library, Fort Rucker, AL 36360 |
| 1 | ATTN: Building 5906-5907 |
| | Commander, U.S.Army Agency for Aviation Safety, Fort Rucker, AL 36362 |
| 1 | ATTN: Technical Library |
| | Commander, Clarke Engineer School Library, 3202 Nebraska Ave., N. Fort Leonard Wood, MO 65473-5000 |
| 1 | ATTN: Library |

| No. of Copies | To |
|---|---|
| | Commander, U.S. Army Engineer Waterways Experiment Station, P.O. Box 631, Vicksburg, MS 39180 |
| 1 | ATTN: Research Center Library |
| | Commandant, U.S. Army Quartermaster School, Fort Lee, VA 23801 |
| 1 | ATTN: Quartermaster School Library |
| | Naval Research Laboratory, Washington, DC 20375 |
| 1 | ATTN: Dr. G. R. Yoder - Code 6384 |
| | Chief of Naval Research, Arlington, VA 22217 |
| 1 | ATTN: Code 471 |
| | Commander, U.S. Air Force Wright Research & Development Center, Wright-Patterson Air Force Base, OH 45433-6523 |
| 1 | ATTN: WRDC/MLLP, M. Forney, Jr. |
| 1 | WRDC/MLBC, Mr. Stanley Schulman |
| | NASA - Marshall Space Flight Center, MSFC, AL 35812 |
| 1 | ATTN: Mr. Paul Schuerer/EH01 |
| | U.S. Department of Commerce, National Institute of Standards and Technology, Gaithersburg, MD 20899 |
| 1 | ATTN: Stephen M. Hsu, Chief, Ceramics Division, Institute for Materials Science and Engineering |
| 1 | Committee on Marine Structures, Marine Board, National Research Council, 2101 Constitution Avenue, N. W., Washington, DC 20418 |
| 1 | Materials Sciences Corporation, Suite 250, 500 Office Center Drive, Fort Washington, PA 19034 |
| 1 | Charles Stark Draper Laboratory, 555 Technology Square, Cambridge, MA 02139 |
| | Wyman-Gordan Company, P.O. Box 8001, North Grafton, MA 01536-8001 |
| 1 | ATTN: Technical Library |
| | General Dynamics, Convair Aerospace Division, P.O. Box 748, Fort Worth, TX 76101 |
| 1 | ATTN: Mfg. Engineering Technical Library |
| | Plastics Technical Evaluation Center, PLASTEC, ARDEC, Bldg. 355N, Picatinny Arsenal, NJ 07806-5000 |
| 1 | ATTN: Harry Pebly |
| 1 | Department of the Army, Aerostructures Directorate, MS-266, U.S. Army Aviation R&T Activity - AVSCOM, Langley Research Center, Hampton, VA 23665-5225 |
| | Department of the Army, Armament Research and Development Center, Dover, NJ 07801 |
| 1 | ATTN: Dr. E. Bloore |

| No. of Copies | To |
|---|---|
| 1 | Department of the Army, Aerostructures Directorate, MS-266, U.S. Army Aviation R&T Activity - AVSCOM, Langley Research Center, Hampton, VA 23665-5225 |
| | GTE Products Corporation, Towanda, PA 18848 |
| 1 | ATTN: Jeff Gonzalez |
| | RARDE, Fort Halstead - Sevenoaks, TN14 7BP Kent, England |
| 1 | ATTN: Dr. Phillip Church |
| | Department of FV&S7, DRA (Chertsey), Chobham Lane, Chertsey, Surrey, England |
| 1 | ATTN: Dr. Anthony Hawkins |
| | National Defense Research Establishment, Box 27322, S-102 54 Stockholm, Sweden |
| 1 | ATTN: Dr. Per-Olof Olsson |
| | Brown University, Division of Engineering, 182 Hope Street, Providence, RI 02912 |
| 1 | ATTN: Prof. Clifton |
| | California Research & Technology, Inc., 5117 Johnson Drive, Pleasanton, CA 94566 |
| 1 | ATTN: Dennis L. Orphal |
| | The Carborundum Company, P.O. Box 1054, Niagra Falls, NY 19302 |
| 1 | ATTN: Robert Palia |
| | Institute for Advanced Technology, 4030-2 West Braker, Austin, TX 78759-5329 |
| 1 | ATTN: Dr. Stephen Bless |
| | University of Dayton Research Institute, KLA14, 300 College Park, Dayton, OH 45469-0182 |
| 1 | ATTN: Dr. N. Singh Brar |
| | University of Dayton, Building JPC 201, Dayton, OH 45469 |
| 1 | ATTN: Mr. David J. Grove |
| | General Dynamics, Land Systems Division, P.O. Box 1800, Warren, MI 48090 |
| 1 | ATTN: Wayne A. Burke |
| | General Research Corporation, 5383 Hollister Avenue, Santa Barbara, CA 93160-6770 |
| 1 | ATTN: Alex Charters |
| 1 | T. L. Menna |
| | Sandia National Laboratories, P.O. Box 5800, Albuquerque, NM 87185 |
| 1 | ATTN: Peter Chen |
| 1 | Dr. Dennis E. Grady, ORG 1533 |
| 1 | Dr. Jack L. Wise |
| | The Pentagon, ODDR&E, Washington, DC 20305 |
| 1 | ATTN: Dr. W. E. Snowden |
| | DARPA/Materials Science Office, 1400 Wilson Boulevard, Arlington, VA 22209-2308 |
| 1 | ATTN: Dr. B. Wilcox |

| No. of Copies | To |
|---|---|
| | Trans Science Corporation, P.O. Box 2727, La Jolla, CA 92038 |
| 1 | ATTN: Dr. G. A. Hegemier |
| | Purdue University, School of Aeronautics & Astronautics, West Lafayette, IN 47907 |
| 1 | ATTN: Dr. Horacio D. Espinosa |
| | University of California - San Diego, Department of Applied Mechanics & Engineering Services - R011, La Jolla, CA 92093-0411 |
| 1 | ATTN: Prof. Sia Nemat-Nasser |
| | DARPA/TTO, 3701 North Fairfax Drive, Arlington, VA 22203-1714 |
| 1 | ATTN: Robert Kocher |
| | Lanxide Armor Products, Inc., 1300 Marrows Road, P.O. Box 6077, Newark, DE 19714-6077 |
| 1 | ATTN: Katherine T. Leighton |
| | University of Hawaii at Monoa, Mineral Physics Group, Department of Geology & Geophysics 255 Correa Road, Honolulu, HI 96822 |
| 1 | ATTN: Prof. Murli Manghnani |
| | Kaman Sciences Corporation, P.O. Box 7463, 1500 Garden of the Gods Road, Colorado Springs, CO 80933 |
| 1 | ATTN: Dr. Michael J. Normandia |
| | Cercom, 1950 Watson Way, Vista, CA 92083 |
| 1 | ATTN: Dr. Rich Palicka |
| | Poulter Laboratory, SRI International, 333 Ravenswood Avenue, Menlo Park, CA 94025 |
| 1 | ATTN: Dr. Donald Curran |
| 1 | Dr. Lynn Seaman |
| 1 | Dr. Donald A. Shockey |
| 1 | Dr. Robert D. Caligiuri |
| | Alliant Techsystems, Inc., 7225 Northland Drive, Brooklyn Park, MN 55428-1515 |
| 1 | ATTN: T. J. Holmquist |
| 1 | Dr. Gordon R. Johnson |
| | E. I. Du Pont de Nemous & Company, Wilmington, DE 19898 |
| 1 | ATTN: Dr. Barry E. Bowen |
| | California Research & Technology, Inc., 5771 Johnson Drive, Pleasanton, CA 94566 |
| 1 | ATTN: Dr. Ronald E. Brown |
| | Aeronautical Research Associates of Princeton, Inc., 50 Washington Road, P.O. Box 2229, Princeton, NJ 08540 |
| 1 | ATTN: Dr. Ross M. Contiliano |
| | Dow Chemical Company, Midland, MI 48640 |
| 1 | ATTN: Mr. Kenneth O. Groves |

| No. of Copies | To |
|---|---|
| | Commander, U.S. Army Tank-Automotive Command, Warren, MI 48397-5000 |
| 1 | ATTN: AMSTA-ZSK |
| 1 | AMSTA-TSL, Technical Library |
| 1 | AMSTA-RSK, Dr. James Thompson |
| | Director, U.S. Army Research Laboratory, Watertown, MA 02172-0001 |
| 2 | ATTN: AMSRL-OP-WT-IS, Technical Library |
| 15 | Author |